

# 1    **The logic of recurrent circuits in the primary visual cortex**

2

3    Ian Antón Oldenburg<sup>1,4,5\*</sup>, William D. Hendricks<sup>1,4\*</sup>, Gregory Handy<sup>2,3\*</sup>, Kiarash Shamardani<sup>1,6</sup>,  
4    Hayley A. Bounds<sup>4</sup>, Brent Doiron<sup>2,3†</sup>, Hillel Adesnik<sup>1,4†</sup>

5    <sup>1</sup>Department of Molecular and Cell Biology, University of California, Berkeley

6    <sup>2</sup>Departments of Neurobiology and Statistics, University of Chicago

7    <sup>3</sup>Grossman Center for Quantitative Biology and Human Behavior, University of Chicago

8    <sup>4</sup>The Helen Wills Neuroscience Institute, University of California, Berkeley

9    <sup>5</sup>Present Address: Department of Neuroscience and Cell Biology, Robert Wood Johnson Medical  
10    School, and Center for Advanced Biotechnology and Medicine, Rutgers University

11    <sup>6</sup>Present Address: Department of Neurology and Neurological Sciences, Stanford University

12    \*equal contributions, †senior authors

13

## 14    **Abstract**

15    Recurrent cortical activity sculpts visual perception by refining, amplifying, or suppressing  
16    incoming visual signals. Despite the importance of recurrent circuits for cortical processing, the  
17    basic rules that govern how nearby cortical neurons influence each other remains enigmatic.  
18    We used two-photon holographic optogenetics to activate ensembles of neurons in Layer 2/3  
19    of the primary visual cortex (V1) in the absence of external stimuli to isolate the impact of local  
20    recurrence from external inputs. We find that the spatial arrangement and the stimulus feature  
21    preference of both the stimulated and the target ensemble jointly determine the net effect of  
22    recurrent activity, defining the cortical activity patterns that drive competition versus  
23    facilitation in L2/3 circuits. Computational modeling suggests that a combination of highly local  
24    recurrent excitatory connectivity and selective convergence onto inhibitory neurons give rise to  
25    these principles of recurrent activity. Our data and modeling reveal that recurrent activity can  
26    have varied impact, but a logic emerges through an understanding of the precise spatial  
27    distribution and feature preference of the multicellular pattern of activity.

## 28    **Introduction**

29           Visual perception involves the coordinated activity of thousands of neurons throughout  
30    the visual system. As the neural representation of sensory stimuli traverse each step of the  
31    visual hierarchy, recurrent circuits at each processing stage transform and refine it (Douglas et  
32    al., 1995; Ko et al., 2011, 2013; Cossell et al., 2015; Lee et al., 2016). Prior experimental and  
33    theoretical work in the primary visual cortex (V1) suggests that recurrent excitation amplifies  
34    responses when signals are weak in order to optimize detection (Douglas et al., 1995; Ko et al.,  
35    2011; Lien and Scanziani, 2013; Cossell et al., 2015; Lee et al., 2016), while recurrent inhibition  
36    suppresses responses when signals are strong to optimize discrimination (Anderson et al., 2000;  
37    Kapfer et al., 2007; Isaacson and Scanziani, 2011; Chettih and Harvey, 2019). Understanding  
38    what patterns of cortical activity drive either amplification or suppression is critical for a  
39    mechanistic understanding of signal transformations in the cortex. However, separating the  
40    impact of local recurrent circuits from the influence of feedforward and feedback inputs during  
41    normal physiological activity is challenging.

42 Past work has focused on isolating recurrent activity by removing feedforward or  
43 feedback activity. Several studies measured feedforward thalamic inputs in isolation by  
44 reversibly silencing the cortex while monitoring incoming visually evoked input using  
45 intracellular recordings (Ferster et al., 1996; Lien and Scanziani, 2013; Li et al., 2013b, 2013a;  
46 Reinhold et al., 2015). Other studies (Nassi et al., 2013; Gómez-Laberge et al., 2016) silenced  
47 higher brain areas through cooling to remove selective feedback to upstream areas and  
48 measured the changes in cortical response to a driving stimulus. In our study we take a  
49 complementary approach: we use high resolution two-photon (2P) holographic optogenetics to  
50 recreate precise experimenter-controlled patterns of neuronal activity and simultaneously  
51 measure the impact across V1 using cellular resolution 2P calcium imaging (Pégard et al., 2017;  
52 Mardinly et al., 2018). With this strategy we probe the functional logic of recurrent cortical  
53 dynamics in the absence of visual driven afferent input and unambiguously determine the  
54 causal impact of different patterns of recurrent dynamics. However, the space of 2P  
55 holographic optogenetic stimulation protocols is immense and care must be taken to  
56 parameterize a sufficiently rich, yet still feasible, probe of the recurrent circuit.

57 There are two main organizing principles that govern recurrent wiring in mouse primary  
58 visual cortex, particularly in Layer (L) 2/3. First, excitatory (E) and inhibitory (I) connectivity falls  
59 off with the physical distance between neurons, so that a majority of recurrent connectivity  
60 comes from neurons that are less than 200  $\mu\text{m}$  apart from one another (Holmgren et al., 2003;  
61 Levy and Reyes, 2012; Billeh et al., 2020; Rossi et al., 2020; Campagnola et al., 2022; Hage et al.,  
62 2022). Second, E to E connectivity is biased to occur between neurons with similar stimulus  
63 feature preferences, such as orientation tuning (Ko et al., 2011; Cossell et al., 2015; Billeh et al.,  
64 2020; Rossi et al., 2020). Many models of cortical circuits, both mathematical and conceptual,  
65 consider either spatial or feature dependent wiring, but few consider how their interaction  
66 determines overall network response. The difficulty rests in the large number circuit  
67 parameters that are needed to construct such a combined circuit model. Further, while  
68 knowledge of monosynaptic connectivity is essential for any predictive model of recurrent  
69 cortical dynamics, it is not sufficient. Both cortical nonlinearities and multi-synaptic paths  
70 complicate the relationship between physical synaptic connections and their functional  
71 influence on a specific pattern of neural activity. The governing hypothesis of our study is that  
72 by designing our 2P optogenetic stimulation protocol to probe the recurrent circuitry defined  
73 by both physical space and feature preference we will uncover the rules by which recurrence  
74 promotes either the recruitment or suppression of cortical activity.

75 Recent work using targeted photostimulation in the presence of a visual stimulus  
76 probed the functional ‘influence’ (Chettih and Harvey, 2019) of putative single neuron  
77 perturbation in V1. They found that co-tuned neurons tended to suppress rather than excite  
78 each other, contrary to a simple prediction from the enriched ‘like-to-like’ connectivity between  
79 excitatory neurons (Ko et al., 2011). Previous rate-based modeling work showed that to  
80 reproduce such strong like-to-like suppression, the network must have strong and specific E to I  
81 connections (Sadeh and Clopath, 2020). Meanwhile, another computational study predicted  
82 that such results would shift and yield like-to-like activation if you adjusted the contrast level of  
83 the stimulus (Cai et al., 2020). These results highlight the importance of measuring and  
84 modeling functional interactions in the intact circuit.

85           Moreover, the influence of a single neuron can be quite different from that of an  
86 ensemble of neurons with coordinated activity, owing to the synaptic wiring rules and  
87 integrative properties of cortical excitatory and inhibitory neurons. Indeed, multi-cell photo-  
88 stimulation has revealed just how diverse functional interactions are in L2/3 (Carrillo-Reid et al.,  
89 2016; Marshel et al., 2019; Russell et al., 2019; Dalgleish et al., 2020). Consequently, creating a  
90 set of generalized organizing principles for the impact and function of L2/3 recurrent circuits  
91 has remained difficult. In particular, the known converging E to I and diverging I to E  
92 connectivity imply that ensemble stimulation of E neurons will be especially potent at recruiting  
93 inhibitory circuits that can have a widespread impact on the remaining cortical network.

94           To define the functional logic of recurrent cortical dynamics in L2/3 of V1 we precisely  
95 photo-stimulated ensembles of excitatory neurons with 2P holographic optogenetics. We  
96 photo-activated ensembles of cells organized along two fundamental axes of the visual  
97 representation: physical space and feature space (orientation). We found that most  
98 perturbations in L2/3 of V1 generated net suppression. However, contrary to these prior  
99 findings, our data reveal two key organizing principles that eluded prior investigation. First, L2/3  
100 recurrent circuits amplify local co-tuned activity by breaking through a recurrent blanket of  
101 suppression, but only on a very local (< 30  $\mu$ m) level. Second, only spatially dense co-tuned  
102 ensembles of L2/3 neurons drive net suppression on this local scale, whereas spatially  
103 distributed co-tuned ensembles drive net excitation. A linear rate-based computational model  
104 captured these key results, but only if we incorporated a wiring rule that combines spatial- and  
105 feature-base synaptic organization. Specifically, we find that the model requires highly local  
106 like-to-like excitatory connections and the convergence of co-tuned excitatory neurons onto  
107 local co-tuned inhibitory neurons. This combination of all-optical circuit interrogation and  
108 detailed computational modeling demonstrate that neural representations in feature space and  
109 physical space intimately interact in the visual cortex. Furthermore, they outline organizing  
110 principles for the functional impact of recurrent cortical dynamics, distinguishing the conditions  
111 for when feedback amplifies input versus when it drives competitive suppression.

## 112 **Results**

113           To determine the role of recurrent activity in L2/3, we used holographic multiphoton  
114 optogenetics to drive small ensembles of L2/3 cells in the absence of visual stimuli thereby  
115 isolating their local network impact. We employed three dimensional scanless holographic  
116 optogenetics with temporal focusing (3D-SHOT) (Pégard et al., 2017; Mardinly et al., 2018) and  
117 leveraged highly potent ultrafast opsins (Mardinly et al., 2018; Sridharan et al., 2022) which  
118 together enable the activation of dozens of cells with near single-cell resolution and millisecond  
119 precision. We simultaneously read out the activity of both stimulated and unstimulated cells  
120 using GCaMP6s. We restricted both the GCaMP6s sensor and the ChroME opsin to excitatory  
121 neurons (see Methods for details) and both imaged and photo-stimulated in 3D to obtain  
122 read/write control over a large fraction of the L2/3 V1 excitatory network. Our general  
123 methodology involved several steps: first, we tested each opsin-expressing neuron for  
124 photosensitivity and tailored the laser power for each cell to ensure reliable activation (see  
125 Methods). Next, we imaged the visual responses of this population to orientated drifting  
126 gratings, determining each neuron's orientation tuning online. Finally, we constructed

127 ensembles of these neurons with varied distributions of net orientation tuning and spatial  
128 locations and targeted these cells for 2P holographic photo-stimulation (for detailed cell  
129 selection criteria, see Methods).

### 130 **Heterogenous inhibition dominates recurrent network effects**

131 We first asked how activating a small number of opsin-expressing L2/3 excitatory cells  
132 (groups of 10 targeted cells) would generally impact overall activity in L2/3 (Fig. 1A-B). Strong  
133 activation of the holographically targeted cells confirmed the efficacy of the optogenetic  
134 approach (Fig. 1C). However, there remains the possibility that stray light could accidentally  
135 activate non-targeted cells. To mitigate the possibility of including such cells in the analysis, we  
136 developed an extensive 3D calibration (see Methods, SFig. 1) resulting in a high-quality optical  
137 point-spread function (PSF) and a physiological PSF, which defined our off target exclusion zone  
138 (see Methods, Fig. 1D). Henceforth, all neurons lying within this exclusion zone are excluded  
139 from analysis. Additionally, by using SepW1-Cre x Camk2a-tTA x tetO-GCaMP6s mice, where  
140 Cre-dependent opsin expression is intentionally sparse, we found only a minimal difference in  
141 nearby activation of opsin-negative cells outside of this exclusion zone (SFig. 2), further backing  
142 our threshold for cell exclusion.

143 Non-targeted neurons displayed a variety of effects, with individual cells responding  
144 distinctly to different ensembles (SFig. 3). However, the majority of cells were suppressed in  
145 response to ensemble stimulation (Fig. 1E-G, SFig. 3B). Across a large set of such experiments  
146 (160 unique 10-cell ensembles in 18 fields of views (FOVs) in 13 different mice) we found that  
147 photo-stimulation suppressed mean population activity (mean effect:  $-0.011 \pm 0.0014 \Delta F/F$ ,  
148  $p < 1e-10$ , Wilcoxon rank sum test, Fig. 1H-I). These results indicate that photo-stimulation of a  
149 small number of L2/3 excitatory neurons recruits net inhibition across the entire population.

150 However, ample evidence suggests that different patterns of neural activity can recruit  
151 distinct recurrent circuits that might preferentially drive either activation or suppression of  
152 activity (Chettih and Harvey, 2019; Marshel et al., 2019). Thus, we next asked whether the  
153 overall sign and magnitude of recurrent activity during holographic photo-stimulation  
154 depended on how the pulses were added to the system. First, we varied the total number of  
155 pulses delivered to a group of 10 targeted neurons between 1 and 50 pulses per cell (~10 to  
156 ~500 total pulses added), while holding the pulse frequency and ensemble size constant (10 Hz  
157 and 10 cells, respectively). We observed net suppression across all these conditions, with a  
158 monotonic increase in suppression with increased number of spikes ( $p < 1.7e-8$ , ANOVA, N=76  
159 Ensembles, 5 FOVs, 2 Mice, SFig. 4A). Next, we varied the stimulation frequency, while holding  
160 ensemble size and total added pulse number constant. In contrast to the previous result,  
161 varying the rate of stimulation did not change the magnitude of the net mean suppression  
162 ( $p > 0.74$  Anova N=46 Ensembles, 2 FOVs, 2 Mice, SFig. 4B). Likewise, varying ensemble size (3-33  
163 cells) while adding a fixed total number of spikes also drove net suppression that did not vary  
164 (mean  $\Delta F/F$ :  $-0.0045 \pm 0.0027$  33 pulses in 3 cells,  $-0.0081 \pm 0.0023$  10 pulses in 10 cells,  $-0.0094$   
165  $\pm 0.0031$  3 pulses in 33 cells,  $p > 0.78$  Anova N=99 Ensembles, 11 FOVs, 5 Mice, SFig. 4C). These  
166 results demonstrate that the primary driver of network suppression is the total number of  
167 added spikes, not the frequency of stimulation nor the size of the ensemble.

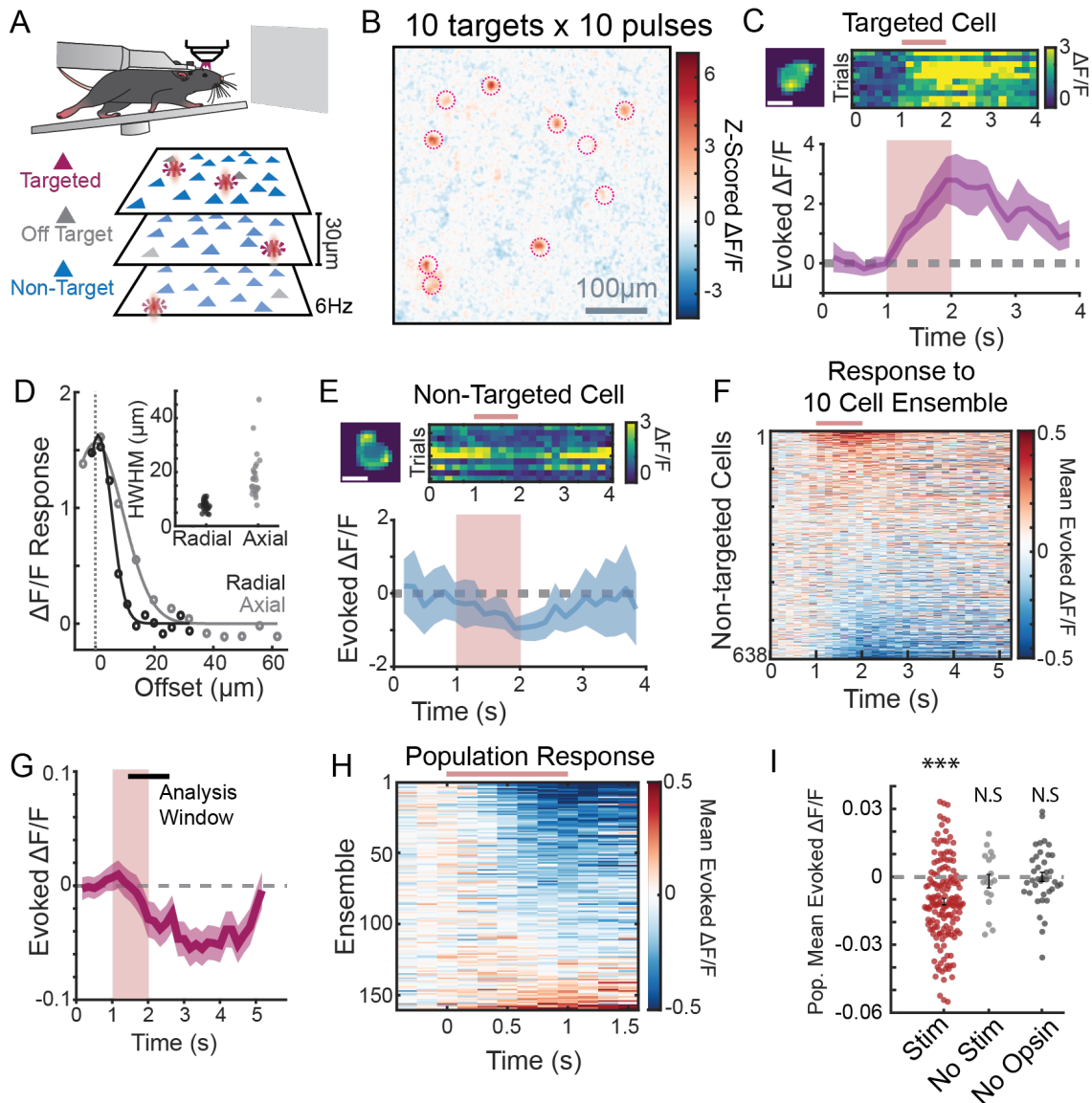


**Figure 1: Stimulation of 10-cell ensembles recruits net inhibition:** **A:** Schematic of the experimental setup. Head-fixed mice are allowed to run on a treadmill while watching a neutral grey screen. Through a cranial window, cells from three planes spaced 30  $\mu\text{m}$  apart are imaged at 6 Hz. Cells from any plane can be targeted for photostimulation (magenta), cells adjacent to photostimulated cells (including offset axially) are categorized as ‘off target’ and excluded (grey), while remaining detected cells are ‘non-target’ cells and used for analysis (Blue). **B:** A representative image superimposing all three planes of imaging during stimulation of a representative 10 cell ensemble. Image pixels are z-scored over the entire recording and averaged by trial type. **C:** Response of a Targeted Cell to photostimulation. Top Left: Image of the cell used in analyses (aka cell mask), scale bar 10  $\mu\text{m}$ . Top Right: heatmap of 10 photostimulation trials, stimulation time noted by maroon bar. Bottom: Mean  $\pm$  95% confidence interval (c.i.) Evoked  $\Delta\text{F}/\text{F}$  from that targeted cell in response to stimulation. Maroon box denotes stimulation time (10 Pulses and 10 Hz). **D:** Representative physiological point spread function (PPSF) radially (black) and axially (grey), aligned to peak (dotted line). Inset PPSFs from 25 cells throughout the field of view. **E:** Response of a Non-Target cell to ensemble stimulation, as in C. **F:** Mean response of 638 non-target cells from a single FOV in response to a representative ensemble stimulation. Cells are sorted based on their response magnitude. Stimulation time noted by maroon bar. **G:** Mean  $\pm$  95% c.i. of all 638 non-target Cells from F. Maroon box indicates stimulation time, black bar indicates analysis window. **H:** Population response, i.e., mean response of all non-target cells, in a field of view to 160 unique 10 cell ensembles. N=160 Ensembles, 18 FOVs, 13 Mice. **I:** Mean population response for each ensemble stimulation (maroon, n=160 Ensembles, 18 FOVs, 13 Mice), no stimulation controls (grey, n=18 FOVs, 13 Mice), or no opsin controls (black, n=38 ensemble, 1 FOV, 1 Mouse). Mean  $\pm$  SEM of condition in black. \*\*\* significantly different from 0, N.S. not significant (Stim  $p < 1.7 \times 10^{-8}$ , No Stim  $p = 0.79$ , No Opsin  $p = 0.96$ ; signed rank test)

169           Based on these results, we focused on the effects of adding 100 total pulses to 10  
170 targeted neurons, which represents a modest perturbation to the system that still drove  
171 reliable and readily quantifiable effects. Importantly, such modest perturbations are well  
172 captured through simulations of associated network models (see below) since they can be  
173 modeled as a linear perturbation around the network's steady state.

174           While it is true that ensemble stimulation leads to suppression *on average* across the  
175 population, there remains significant heterogeneity of response, with a significant number of  
176 neurons showing activation rather than suppression. Specifically, we found  $2.34 \pm 0.09\%$  of  
177 non-targeted cells were significantly activated (i.e., 99% CI excludes 0, false discovery rate 1%)  
178 and  $5.58 \pm 0.19\%$  of non-targeted cells were significantly suppressed (SFig. 3B-C). The central  
179 goal of this study is to explain this heterogeneity based on the joint physical and feature space  
180 properties of the neurons both in the stimulated ensemble and recorded populations.

### 181 **Cortical space organizes the impact of recurrent dynamics**

182           Physical space in the sensory neocortex represents a fundamental axis of circuit  
183 organization owing to both the topographic mapping of sensory inputs onto cortical tissue and  
184 the anatomy of cortical neurons (Dräger, 1975; Wagor et al., 1980; Garrett et al., 2014; Zhuang  
185 et al., 2017). Thus, we hypothesized that the sign, scale, and magnitude of recurrent circuit  
186 influence might vary substantially with distance from the targeted ensemble. To test this, we  
187 quantified the impact of ensemble photo-stimulation as a function of distance from each  
188 targeted location and ensemble (see Methods). Indeed, we found that despite the overall mean  
189 suppression described above, cells proximal to the stimulated ensemble but outside of the off  
190 target exclusion zone were reliably activated, while cells further away from a target were  
191 suppressed ( $< 30 \mu\text{m}$  from a target mean  $\Delta F/F: 0.044 \pm 0.005$ ,  $p < 1.1 \times 10^{-10}$ ;  $50\text{-}150 \mu\text{m}$  from a  
192 target mean  $\Delta F/F: -0.013 \pm 0.001$ ,  $p < 4.0 \times 10^{-17}$ , Signed Rank Test; Fig. 2A). Beyond that distance,  
193 the sign of the modulation stayed negative and slowly returned to zero as the distance  
194 increased.

195           This spatial pattern of nearby excitation and surround inhibition characterizes the  
196 spatial response function of a minimal recurrent circuit and has often been considered as a  
197 basis for lateral competition in the cortex (Cavanaugh et al., 2002; Derdikman et al., 2003; Kang  
198 et al., 2003; Isaacson and Scanziani, 2011; Adesnik et al., 2012; Shushruth et al., 2012).  
199 Phenomenologically, it can be captured as the difference of a narrow excitatory and a broader  
200 inhibitory gaussian spatial function (Fig. 2A, solid line; excitatory spread:  $22 \mu\text{m}$ , inhibitory  
201 spread:  $147 \mu\text{m}$ ). Moreover, these experiments demonstrate that activation of even a small  
202 number of L2/3 excitatory neurons is sufficient to generate this 'check-mark' shape. However,  
203 exact mechanistic circuit basis giving rise to this shape remains unclear.

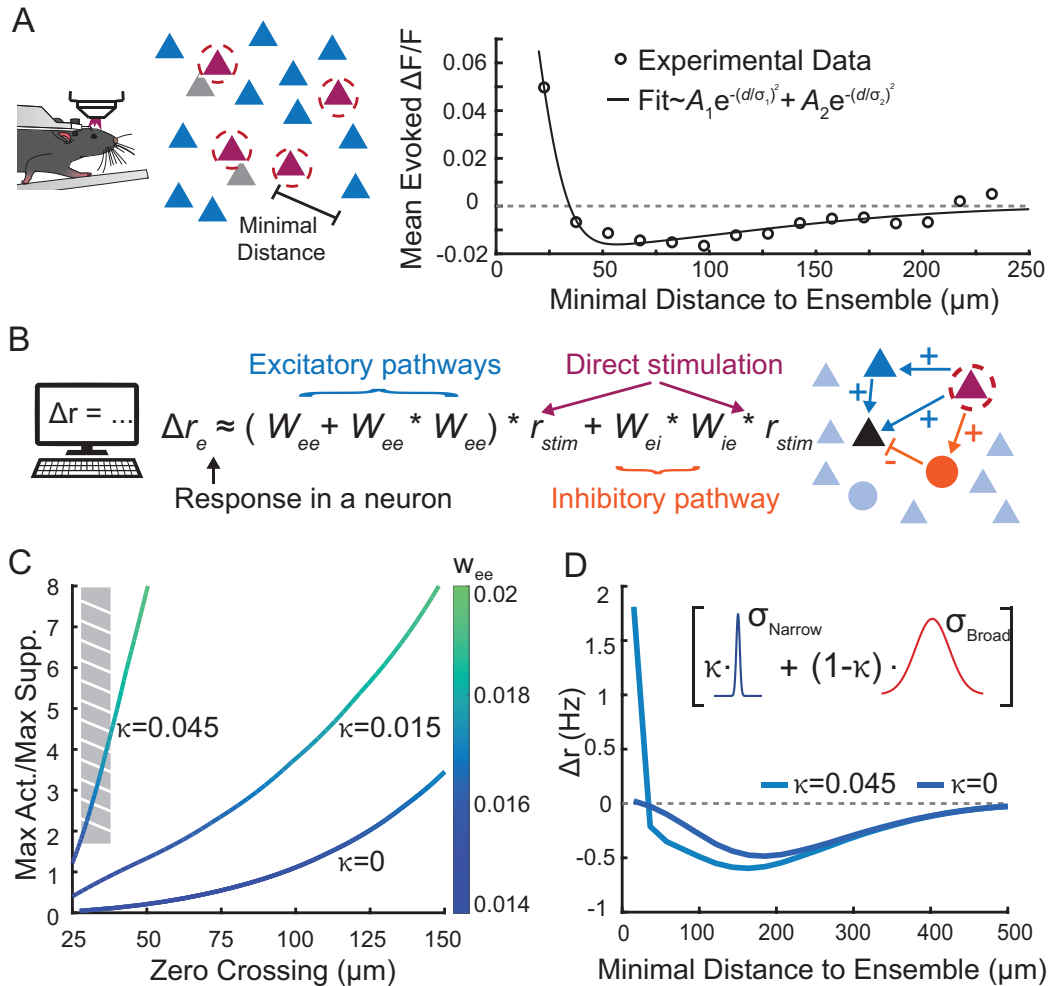


**Figure 2: Decomposing population responses reveals nearby activation and surround suppression.** **A:** Left: Schematic of the minimal distance metric for non-target cells (magenta: targeted cells, gray: off-target cells, blue: non-targeted cells). Right: Non-targeted cell responses to optogenetic stimulation as a function of minimal distance to ensemble (open circles) fitted to a sum of Gaussian spatial functions ( $A_1 = 0.1956$ ,  $\sigma_1 = 22.07 \mu\text{m}$ ,  $A_2 = -0.021$ ,  $\sigma_2 = 147.31 \mu\text{m}$ ). Cells near the stimulated ensemble were reliably activated, while cells further away from a target were suppressed ( $<30 \mu\text{m}$  from a target mean  $\Delta F/F: 0.044 \pm 0.005$ ,  $p < 1.1 \times 10^{-10}$ ;  $50-150 \mu\text{m}$  from a target mean  $\Delta F/F: -0.013 \pm 0.001$ ,  $p < 4.0 \times 10^{-17}$ , Signed Rank Test). Bin sizes are  $15 \mu\text{m}$ . **B:** Schematic of all monosynaptic and disynaptic pathways resulting in a change in the baseline firing rate (blue: excitatory pathways, orange: inhibitory pathways). \* denotes convolution in space. **C:** The zero crossing and relative strength of nearby excitation (max activation / max suppression) as a function of recurrent excitatory strength ( $w_{ee}$ ) and biased connections on the narrow spatial scale ( $\kappa$ ). The gray stripe box indicates the experimentally observed data regime and illustrates the need of the additional spatial to capture the nearby excitation observed in the data. **D:** Non-targeted cell responses in the model as a function of minimal distance to ensemble for different values of  $\kappa$ . Inset: schematic show the narrow vs. broad spatial scales in the model (see Methods for more details).

204 To address this question, we developed a computational model of these targeted  
 205 optogenetic perturbations (see Methods). Our goal was to understand how connectivity  
 206 principles in L2/3 recurrent circuits could explain why recurrent activation is extremely local but  
 207 why suppression dominates at larger distances from the stimulated ensemble. We wired the  
 208 simulated circuit based on previously acquired connectivity data (Rossi et al., 2020; SFig. 5A-D),  
 209 and modeled the dynamics of the population with a two-dimensional neural field model (Huang  
 210 et al., 2019, see Methods). Due to the modest size and strength of the optogenetic  
 211 perturbations we considered the network response as linear perturbations around a steady

212 state firing rate solution. Further, because the experiments were performed in absence of  
213 a visual input, we could assume that the neurons in the network have a low gain response,  
214 implying that the effective connectivity strength is relatively weak. This allowed us to  
215 investigate the network perturbation via a synaptic pathway expansion with just a few terms  
216 (Ocker et al., 2017; Sadeh and Clopath, 2020). Specifically, we considered monosynaptic and  
217 disynaptic excitatory connections ( $E \rightarrow E$  and  $E \rightarrow E \rightarrow E$ ) and disynaptic inhibitory connections  
218 ( $E \rightarrow I \rightarrow E$ ) (Fig. 2B).

219 After fitting the spatial components of the model (see Methods), we are left with two  
220 free parameters that correspond to the strengths of these pathways:  $w_{ee}$  (the effective strength  
221 of  $E \rightarrow E$  connections) and  $w_{eie}$  (the effective strength of the inhibitory pathway). We find that  
222 nearby excitation and surround inhibition arises for a variety of parameter values, with near  
223 identical shapes arising for fixed values of  $w_{ee}/w_{eie}$ . After fixing  $w_{eie}$  and varying  $w_{ee}$  for  
224 simplicity, we find that we can adjust both the zero crossing of this curve and the strength of  
225 the nearby excitation (Fig. 2C). However, we see that this model is unable to pass through the  
226 experimentally observed data regime (Fig. 2C, gray box, SFig. 5E, see Methods). Specifically,  
227 when these parameters are adjusted to match the experimental observed cross at  $\sim 35 \mu\text{m}$ , the  
228 model fails to capture the relative strength of nearby excitation to more distant suppression. To  
229 capture this key detail, we reasoned that we needed to add an additional spatial scale to the  
230 model (Fig. 2D). Based on recent work (Kwan and Dan, 2012; Kondo et al., 2016; Ringach et al.,  
231 2016; Yu et al., 2020), L2/3 neurons in mouse V1 have unique connectivity rules on a narrow  
232 spatial scale of ( $< 50 \mu\text{m}$ ) leading to small columnar structures that is not strictly a salt-and-  
233 pepper organization. Adding in such a tight spatial component (i.e.,  $\kappa > 0$ , see Methods) allowed  
234 the model to simultaneously capture both the nearby excitation and the appropriate zero  
235 crossing between excitation and suppression.

236 Similar to how different sensory stimuli will drive different spatial distributions of  
237 activity, we next asked how the spatial distribution of targeted cells would impact either the  
238 suppression or activation of recurrent activity. To investigate this question experimentally, we  
239 activated ensembles of 10 neurons that were either distributed or clustered in space (see Fig.  
240 3A). Indeed, we found that activating a spatially compact ensemble drives much more surround  
241 inhibition than stimulating a spatially diffuse ensemble (linear regression of mean  $\Delta F/F$  vs  
242 spread slope:  $1.3e-4 \Delta F/F$  per  $\mu\text{m}$  spread,  $p < 1.4e-5$ ; Fig. 3A). In contrast, the spread of the  
243 ensemble did not alter nearby excitation (linear regression of mean  $\Delta F/F$  vs spread slope:  $3.5e-$   
244  $5$ ,  $p = 0.57$ ; SFig. 6A-C). More precisely, and in line with our computational model, the level of  
245 surround inhibition (at  $50-150 \mu\text{m}$ ) increased as the spatial distribution of the ensemble's  
246 component neurons decreased (Fig. 3B). To understand what accounts for this, we examined in  
247 the model the relative strength of the  $E \rightarrow E$  and  $E \rightarrow I \rightarrow E$  pathways as a function of the spatial  
248 spread of the ensemble. We found that as the ensemble spread decreases, both synaptic  
249 pathways increase in magnitude, but the strength of inhibitory pathway increases faster,  
250 leading to the observed effect (Fig. 3C; slope is  $\sim 9\%$  greater for the inhibitory pathway).

251 These findings are consistent with the idea that strong inhibition derives from the  
252 convergence of excitatory activity onto individual inhibitory neurons. In the case of a spatially  
253 compact ensemble individual inhibitory neurons receive input from multiple directly stimulated

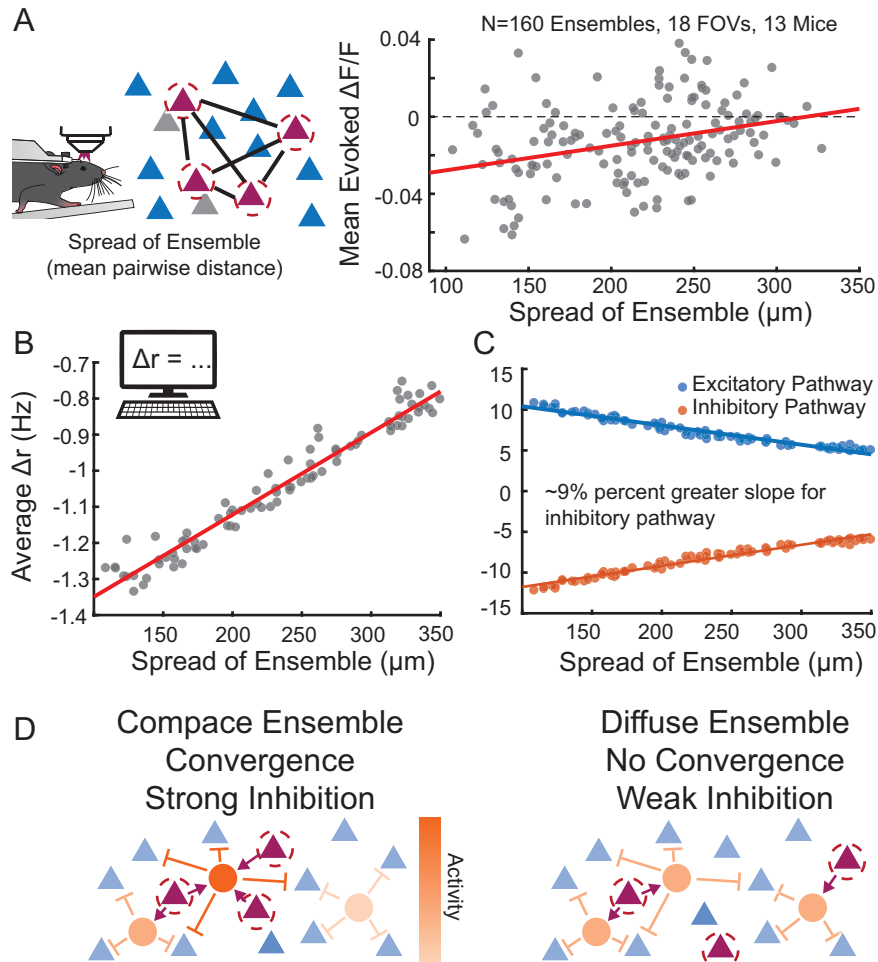


**Figure 3: Tight ensembles recruit stronger network suppression because of converging inhibitory pathways.** **A:** Left: Schematic of ensemble spread metric (mean pairwise distance). Right: Non-targeted cell responses averaged across the population ( $N=160$ ) for ensembles with different spreads. Activating a spatially compact ensemble drives more surround inhibition than stimulating a spatially diffuse ensemble (linear regression of mean  $\Delta F/F$  vs spread slope:  $1.3e-4 \Delta F/F$  per  $\mu\text{m}$  spread,  $p < 1.4e-5$ ). **B:** Same as A except for the network model. **C:** Strength of the model excitatory (blue) and inhibitory (red) pathways as a function of ensemble spread, showing that as the ensemble spread decreases, the inhibitory pathway shows a greater level of recruitment. **D:** Schematics illustrating the ability of the targeted cells to activate inhibitory pathways via convergences for compact (left) and diffuse (right) ensembles.

254 cells. These super activated inhibitory cells then feedback divergently inhibiting the entire  
 255 network (Fig 3D).

### 256 Feature space organization of the impact of recurrent dynamics

257 In addition to physical space, feature space represents a second axis of the functional  
 258 organization of cortical circuits. In mouse V1, orientation-tuning is a crucial feature that is not  
 259 structured in physical space, unlike the orientation columns and pinwheels of monkeys, cats,  
 260 and other species (Ohki et al., 2005; Ohki and Reid, 2007; Bonin et al., 2011). Despite the lack of  
 261 local organization, feature space is known to influence both synaptic connectivity and the  
 262 functional influence of individual neurons in mouse V1 (Ko et al., 2011; Cossell et al., 2015;  
 263 Chettih and Harvey, 2019). However, as most reports focus on the impact of individual neurons,  
 264 it is unknown if multiple neurons defined in feature space synergize to drive recurrent activity.  
 265 One hypothesis is that a co-tuned (i.e., iso-oriented) group of excitatory neurons, analogous to

266 spatial clustering in orientation space, should drive strong network activity due to convergent  
 267 excitation onto the same postsynaptic excitatory cells (Marshall et al., 2019).

268 To test this hypothesis, we presented mice with a randomized series of full screen  
 269 drifting gratings each trial presenting one of 8 cardinal directions of motion and calculated  
 270 tuning curves for each neuron online, generating ensembles of cells varying in preferred-  
 271 orientation and orientation selectivity. We summarized the selectivity of an ensemble using an  
 272 'ensemble OSI', i.e., the OSI of the average of the tuning curves (see Methods, Fig. 4A-B). To  
 273 optimally select exemplar ensembles (among the  $\sim 10^{23}$  possible ensembles – 1,000 choose 10)  
 274 we created a discrete optimizer (see Methods) that designs distinct ensembles by automatically  
 275 choosing eligible cells that fall within a targeted spatial and OSI range. We used this optimizer

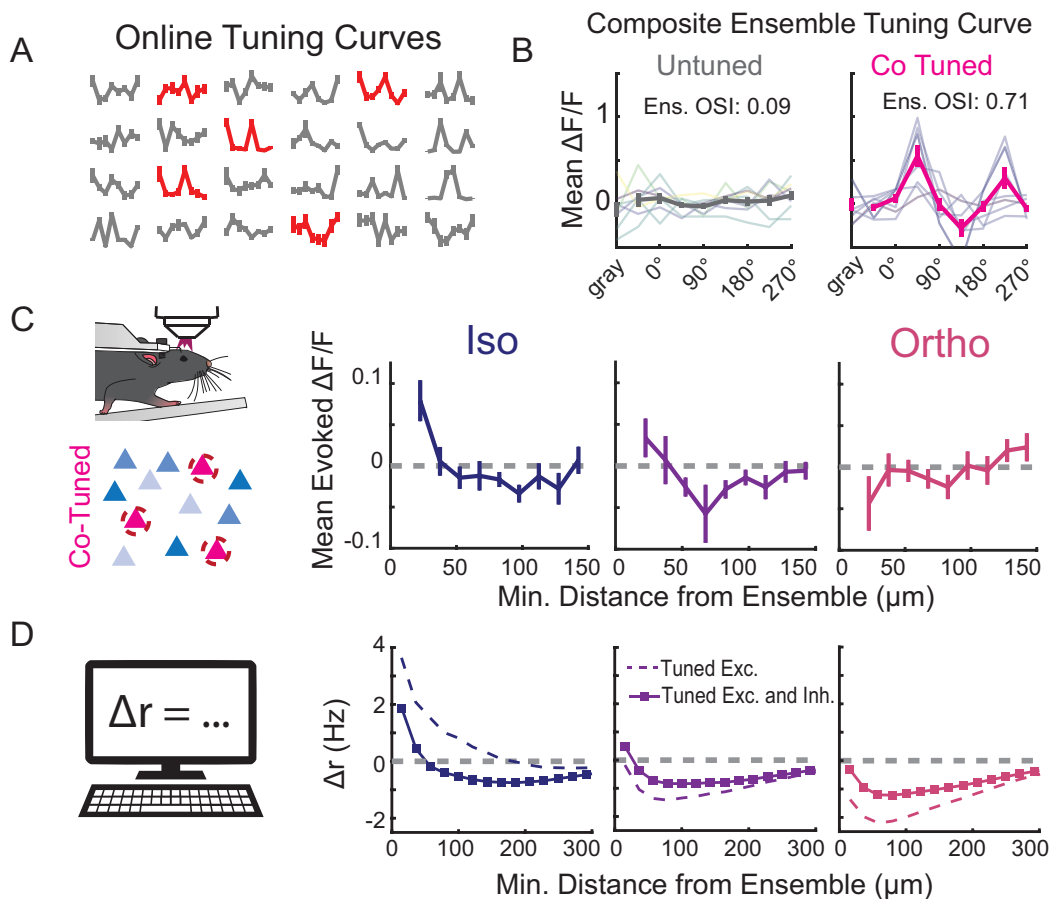


**Figure 4: Relative tuning of non-targeted cells determines response to stimulated ensembles.** **A:** Representative online tuning curves from 24 non-targeted cells. Each point of each curve is the mean  $\pm$  SEM normalized Ca response to a drifting visual grating. Red cells indicate cells that were selected for an individual ensemble. **B:** Two representative composite ensemble tuning curves, i.e., the mean of the tuning curves of the 10 cells that make up an ensemble, are shown. Left a representative untuned ensemble (low ens. OSI), right a representative co-tuned ensemble (high ens. OSI). Individual tuning curves lighter colors, mean  $\pm$  SEM dark bold colors. **C:** Left: Schematic showing a co-tuned ensemble. Right: Non-targeted cell responses  $\pm$  SEM as a function of their minimal distance to the ensemble according to their relative tuning with the stimulated ensemble (Left:  $\Delta\theta = 0^\circ$  (Iso), Middle:  $\Delta\theta = \pm 45^\circ$ , Right:  $\Delta\theta = 90^\circ$  (Ortho)). The included cells were responsive to visual stimuli ( $p$ -value  $< 0.05$ ) and tuned (OSI  $> 0.25$ ). Nearby iso-oriented cells ( $< 30 \mu\text{m}$ ) are activated dramatically more than those cells that prefer orthogonal stimuli ( $p < 0.0035$ , Wilcoxon one-sided ranked sum test,  $N=17$  Ensembles, 8 FOVs, 3 Mice). Bin sizes are  $15 \mu\text{m}$ . **D:** Same as C, except for the network model with (solid) and without (dashed) tuned E $\rightarrow$ I connections.

276 to ensure that the chosen ensembles were evenly distributed across feature (orientation)  
277 space. Surprisingly, we found that ensembles with higher ensemble OSI did not generate  
278 greater network effects when averaged across all non-targeted neurons (SFig. 6D-F, no  
279 significant correlation between ensemble OSI vs the total population response,  $p = 0.26$  linear  
280 regression; or between ensemble OSI and nearby, mid distance, or far cells' responses;  
281  $p=0.084$ ,  $p=0.27$ , and  $p=0.89$  respectively by linear regression).

282 Based on the principle of selective like-to-like connectivity, we next asked whether co-  
283 tuned ensembles might preferentially impact non-targeted neurons that share feature  
284 preference. To test this hypothesis, we restricted our analysis to the 'co-tuned ensembles' and  
285 divided the non-stimulated cells based on their relative preferred orientation. Such a 'co-tuned  
286 ensemble' consisted of individually tuned members (mean OSIs of ensemble members  $>0.5$ )  
287 with similar tuning preferences (ensemble OSI  $>0.7$ ). We find that nearby cells ( $<30\mu\text{m}$ ) that  
288 also prefer the same orientation as the stimulated ensemble (i.e., iso-oriented cells), are  
289 activated dramatically more than those cells that prefer orthogonal stimuli ( $p<0.0035$ , Wilcoxon  
290 one-sided ranked sum test,  $N=17$  Ensembles, 8 FOVs, 3 Mice, Fig. 4C). Strikingly, these nearby  
291 orthogonally oriented cells were instead highly suppressed. These results demonstrate that the  
292 organization of an ensemble in feature space – in this case orientation preference – profoundly  
293 influences its recurrent impact on specific cells in the cortical network.

294 To explain this switch from like-to-like excitation to like-to-unlike suppression, we used  
295 our computational model to determine which features of circuit connectivity are required to  
296 generate it. We considered three hypotheses: (1) the orientation dependence of recurrent  
297 inputs could emerge on their own based purely spatial connectivity rules and salt-and-pepper  
298 orientation tuning, (2) like-to-like  $E \rightarrow E$  connectivity but random  $E \rightarrow I$  and  $I \rightarrow E$  connectivity could  
299 explain it, or (3) orientation specificity would be required in all of these pathways. In line with  
300 prior work, we assumed that the orientation preferences of individual neurons are inherited  
301 from feedforward projections and not spatially organized.

302 When synaptic connectivity only followed a spatial wiring rule with no specificity in  
303 orientation space, we found no difference in the recruited recurrent activity of iso-oriented vs.  
304 orthogonally oriented neurons (SFig. 7), demonstrating that pure spatial rules are not sufficient  
305 on their own to explain the experimentally observed recurrent dynamics. Adding in like-to-like  
306 connectivity between excitatory neurons (Ko et al., 2013; Rossi et al., 2020) reproduced  
307 orientation-preference dependent effects, qualitatively similar to the experiment results (Fig.  
308 4D; dashed). Specifically, cells that were iso-oriented to the photo-stimulated tuned ensemble  
309 showed excitation, while those that are orthogonally orientated showed suppression. However,  
310 the model with this wiring scheme substantially overestimated iso-oriented excitation and  
311 orthogonally oriented suppression at all distances, and completely failed to capture the iso-  
312 oriented surround inhibition beyond  $50\mu\text{m}$ . Finally, when the model incorporated like-to-like  
313 excitatory-to-inhibitory and inhibitory-to-excitatory connections, as recently suggested by  
314 (Znamenskiy et al., 2018), it accurately reproduced the experimental data both qualitatively and  
315 quantitatively (Fig. 4D; solid). These results imply that feature-specific synaptic connectivity  
316 across all three synaptic pathways is essential to explain the space and feature-dependence of  
317 recurrent cortical dynamics.

## 318 **Interactions between physical space and feature space**

319 Thus far, we have only considered how the geometric distribution (Fig. 3) and feature  
320 preferences of an ensemble (Fig. 4) govern cortical recurrent dynamics independently.  
321 However, since sensory stimuli will necessarily recruit recurrent dynamics that vary jointly  
322 across these two dimensions, we hypothesized that the spatial distribution and feature  
323 preference of an ensemble should interact to determine the resultant impact of ensemble  
324 photo-stimulation on the cortical network. To investigate this hypothesis, we used the discrete  
325 optimizer to identify co-tuned or untuned ensembles that were either spatially compact or  
326 spatially distributed and photo-stimulated them while observing the activity of the non-target  
327 cells. First, we found that the spatial spread of an un-tuned ensemble (ensemble OSI  $< 0.3$  and  
328 mean OSIs of ensemble members  $< 0.5$ , see Methods) did not affect its net recurrent impact,  
329 such that for both spatially compact and diffuse ensembles we observed the characteristic  
330 nearby excitation and surround inhibition when computed across all non-targeted neurons (Fig.  
331 5A, grey traces). However, the spatial spread of a co-tuned ensemble profoundly influenced its  
332 recurrent effects: compact, co-tuned ensembles generated no nearby excitation and instead  
333 showed nearby suppression, whereas a spatially diffuse co-tuned ensemble generated the  
334 more typical center/surround effects (Fig. 5A, pink and purple traces; nearby activity co-tuned,  
335 close ensemble ( $N = 8$ ) vs. co-tuned far ensemble ( $N=17$ )  $p < 0.008$ , Wilcoxon one-sided ranked  
336 sum test).

337 This result appears at odds with previous optogenetic results, which have suggested  
338 that a co-tuned ensemble should evoke a population response reminiscent of a visual image  
339 containing a drifting grating (Marshall et al., 2019). To reconcile these results, we asked how the  
340 activity of visually responsive cells varied across spatially diffuse and compact co-tuned  
341 ensembles, as a function of their orientation preference (Fig. 5B-C). We observed that diffuse  
342 co-tuned ensembles recruited very little nearby suppression in neurons at any orientation. In  
343 contrast, compact co-tuned ensembles, activated nearby iso-oriented cells, while nearby cells  
344 at other orientations were reliably suppressed. Further, non-visually responsive cells were also  
345 suppressed during the stimulation of such ensembles. In total, these data suggest that compact,  
346 co-tuned ensembles were able to sharpen the input signal locally, activating iso-oriented cells  
347 while suppressing all other cells. Diffuse co-tuned ensembles, however, lacked this ability to  
348 significantly suppress nearby 'unlike' cells.

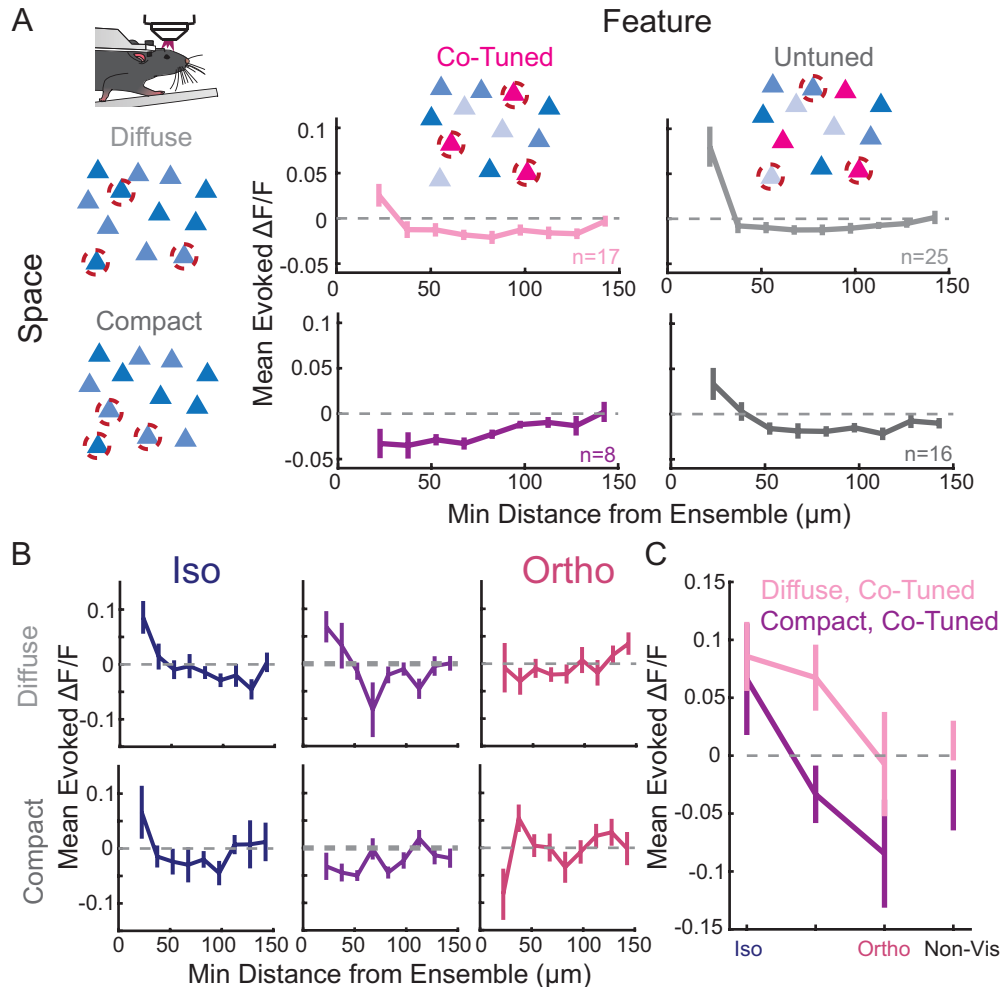


**Figure 5: Space and feature properties of the stimulated ensemble shape the population responses.** **A:** Ensembles are divided by two categories, whether they are diffuse (mean distance  $> 200 \mu\text{m}$ , top) or compact ( $< 200 \mu\text{m}$ , bottom) vs co-tuned (Ens. OSI  $> 0.7$ , Left) or Untuned ( $< 0.3$ , Right). Non-targeted cell responses  $\pm$  SEM as a function of their minimal distance to the ensemble. **B:** Co-tuned ensembles divided by mean separation (as in A), but non-targeted cells are separated by relative tuning with the stimulated ensemble (Left:  $\Delta\theta = 0^\circ$  (Iso), Middle:  $\Delta\theta = \pm 45^\circ$ , Right:  $\Delta\theta = 90^\circ$  (Ortho)). **C:** Non-targeted cell responses from the first bin of panel B as a function of their relative tuning with the stimulated co-tuned ensembles.

349 To unpack these results further, we turn again to our computational model, which now  
 350 consists of both the spatial- and feature-based wiring rules necessary to reproduce our core  
 351 experimental findings. Indeed, simulations showed that a diffuse, co-tuned ensemble  
 352 generated effects that are similar to previous results: nearby excitation and suppression  
 353 inhibition (Fig. 6A; pink curve), while compact, co-tuned ensembles drove suppression across all  
 354 distances (Fig. 6A; magenta curve). Decomposing this result into the direct excitatory and  
 355 disinhibitory pathways, we found that while the compact ensemble recruits both more  
 356 inhibition and more excitation than a diffuse ensemble (Fig. 6B), however, inhibition tends to  
 357 dominate the net effects on firing rates. This observation illustrates an interesting tradeoff  
 358 between the  $E \rightarrow I \rightarrow E$  inhibitory pathway and the excitatory pathways as one compresses the co-  
 359 tuned ensemble. Namely, nearby suppression replaces nearby excitation as the ensemble  
 360 shrinks in space.

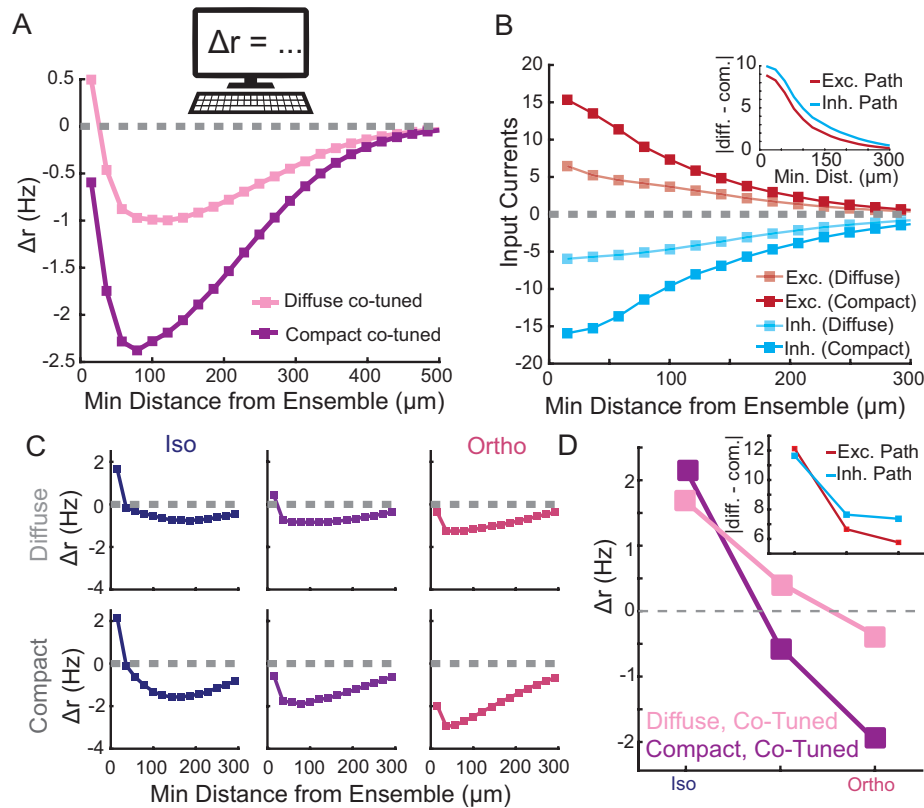


**Figure 6: Network model with both spatial- and feature-based tuned connections wiring rules can recapitulate core experimental results.** **A:** Non-targeted cell responses in the network model as a function of their minimal distance to the ensemble according to the ensemble spread and tuning. **B:** The excitatory (red) and inhibitory (blue) input pathways for the spatially diffuse and compact co-tuned ensembles. Inset: Absolute difference of excitatory and inhibitory paths showing that while both pathways increase in magnitude for compact ensembles, the inhibitory pathway shows a larger increase. **C:** Non-targeted cell responses in the network model as a function of their minimal distance to the ensemble according to their relative tuning with the stimulated co-tuned ensembles. **D:** Non-targeted cell responses from the first bin of panel C as a function of their relative tuning with the stimulated co-tuned ensembles. Inset: Absolute difference of excitatory and inhibitory pathways.

361 After decomposing these effects based on the orientation preference of the non-  
 362 targeted neurons, we find that the model continues to agree with our experimental results:  
 363 compact, co-tuned ensembles sharpen the input signal locally more so than diffuse, co-tuned  
 364 ensembles (Fig. 6C and 6D). Again, we can decompose this result into the two pathways, and  
 365 again we find that it is the stronger recruitment of the inhibitory pathway, in this case via cells at  
 366 non-iso orientations, that lead to this result (Fig. 6D, inset).

### 367 Discussion

368 Recurrent activity in V1 could serve to amplify sensory input when signals are weak  
 369 (Douglas et al., 1995; Ferster et al., 1996; Ichida et al., 2007; Ko et al., 2011; Lien and Scanziani,  
 370 2013; Li et al., 2013b; Cossell et al., 2015; Lee et al., 2016), but drive competition among stimuli  
 371 when signals are strong (Anderson et al., 2000; Kapfer et al., 2007; Isaacson and Scanziani,  
 372 2011; Chettih and Harvey, 2019; Mossing et al., 2021). However, as definitively isolating the  
 373 role of recurrent circuits from the impact of feedforward or feedback input has not been  
 374 feasible, fundamental concepts on the role of recurrent activity in cortical computation remain  
 375 untested. By selectively activating small ensembles of L2/3 cells in the absence of visual input

376 we could isolate the role of local recurrent activity using multiphoton holographic optogenetics  
377 and calcium imaging. By leveraging our ability to design unique ensembles of L2/3 neurons  
378 whose properties varied across both physical space and feature space, we systemically tested  
379 the role these two fundamental axes have in driving recurrent activity. Moreover, by combining  
380 this experimental approach with detailed computational modeling, we proposed a wiring rule  
381 that depends on both spatial and feature properties of cells and investigated the implications of  
382 such a rule.

383 We found that recurrent circuits could either amplify or suppress cortical activity  
384 depending on the spatial distribution and tuning of the presynaptic ensemble and the location  
385 and tuning of the postsynaptic cells. The vast majority of photo-stimulation patterns led to net  
386 suppression of cortical activity, but the sign, scale and magnitude of recurrent network  
387 modulation followed a specific logic. For example, we found that compact, co-tuned ensembles  
388 largely drive suppression, while spatially distributed co-tuned neurons drive amplification, but  
389 only of nearby neurons, otherwise they likewise drive suppression. Taken together, our results  
390 demonstrate that the recurrent circuitry defined by feature space and physical space jointly  
391 determine the impact of recurrent circuits.

392 Importantly, we used relatively modest perturbations (~10 action potentials added to  
393 ~10 neurons) to avoid pushing the system out of its physiological operating range. Further,  
394 from a computational perspective, modest perturbations are easier to interpret since they  
395 evoke small deviations from the steady-state firing rate solution. Indeed, we were able to  
396 construct network simulations with few parameters that could accurately capture our initial  
397 experimental results and qualitatively predict further experimental outcomes. Investigation of  
398 the model suggested that like-to-like connectivity not only between excitatory neurons, but  
399 also between excitatory and inhibitory neurons, was important for explaining the results. A  
400 narrow spatial scale of like-to-like E→E connectivity, as suggested previously (Kwan and Dan,  
401 2012; Ringach et al., 2016; Yu et al., 2020), was likewise essential for accurately predicting the  
402 experimental data.

403 Several recent studies have also use 2P optogenetics to probe functional connectivity in  
404 mouse visual cortex. One recent study (Marshall et al., 2019) found that optogenetic stimulation  
405 of tuned ensembles in mouse V1 primarily generated recurrent amplification of co-tuned  
406 activity. Under most conditions in our data, suppression dominates, with recurrent excitation  
407 confined to a close distance to targeted cells. One possible explanation for this apparent  
408 discrepancy is that we deliberately made smaller perturbations of co-tuned ensembles limited  
409 to about ten neurons, while this other study aimed to recruit larger numbers of neurons and  
410 possibly at higher firing rates. It is possible that increasing the number of photo-stimulated  
411 neurons in the co-tuned ensemble in our experiments would increase excitation relative to  
412 inhibition which could lead to net amplification. However, more generally, since we found that  
413 net impact of recurrent circuits depends on several key properties of the neural activity pattern,  
414 it is also possible that if this other study took these factors into account our results could be in  
415 more agreement.

416 Two recent studies in mouse V1 either targeted single (Chettih and Harvey, 2019) or  
417 multiple (Russell et al., 2019) neurons in L2/3 with 2P photostimulation largely generated

418 suppression across the network, but also some nearby excitation. While this appears to better  
419 match our results, these studies also observed much more substantial like-to-like suppression,  
420 leading one of the studies to hypothesize that recurrent networks are primed for competition  
421 rather than amplification (Chettih and Harvey, 2019). However, there are two key differences  
422 between this study's approach and the one we used here. First, they targeted single neurons  
423 rather than ensembles (Chettih and Harvey, 2019). Since most synapses in cortex are weak, the  
424 impact of adding spikes to one neuron could be substantially different than when activating  
425 ten. For example, cortical somatostatin cells, which are a major source of recurrent inhibition in  
426 L2/3, are only recruited effectively by the activation of two or more L2/3 pyramidal cells (Kapfer  
427 et al., 2007). Additionally, the notion of compact versus diffuse nature of an ensemble, which  
428 we found to be a critical determinant of net impact, has no meaning for single-neuron  
429 perturbations and was not explored in Russell et al. (2019).

430 Furthermore, both aforementioned studies conducted their experiments while  
431 presenting visual stimuli to the animal. This may have been necessary to make it possible to  
432 measure the very small effects of single-neuron photo-stimulation (Chettih and Harvey, 2019)  
433 or influence behavioral performance (Russell et al., 2019), yet it also means the network was in  
434 a state that was potentially dominated by non-recurrent sources of input. This could shift the  
435 dynamical state of network, and potentially lead to a stronger recruitment of suppression.  
436 Finally, the magnitude and sign of the like-to-like modulation was not computed across  
437 different distances from the optogenetically targeted neuron (Chettih and Harvey, 2019). Since  
438 we also found that this distance was a key modulator of like-to-like effects, it is possible that  
439 such analysis might reveal better agreement with our data.

440 Perhaps one key issue with comparing results of 2P optogenetic targeting across studies  
441 is the enormous potential parameter space of the perturbations. These include the number,  
442 spacing and featuring tuning of the targeted neurons, but also the precise temporal pattern of  
443 optically evoked activity and total number of spikes. Some of these are readily under user-  
444 control (such as the spacing of the targeted neurons, the number of pulses delivered to each  
445 neuron) and some are often not, such as the exact number of neurons that are actually photo-  
446 stimulated and the temporal pattern of their activity. Additionally, the optical approach and the  
447 microbial opsin used can profoundly influence the pattern and magnitude of activity.  
448 Standardizing these parameters should aid in better comparison. More generally, using an  
449 approach that ensures specific numbers and temporal patterns of the evoked spikes, as  
450 recently described, should obviate the need for matching these parameters.

451 With respect to our computational modeling, a similar study (Sadeh and Clopath, 2020)  
452 also made use of a linear rate-based model to explore the pathways driving recurrent circuit  
453 impacts during photo-stimulation of a small number of neurons. Like this study, we also found  
454 that the E→I pathway must be sufficiently strong and feature-specific to explain the large  
455 amount of suppression observed. However, this previous study largely focused on explaining  
456 how the optogenetic perturbation of a single cell influences recurrent activity. Here, we were  
457 able to further develop a model that simultaneously incorporates space- and feature-based  
458 wiring rules due to the larger number of neurons in the stimulated ensemble. Specifically, by  
459 exploring different spatial distributions of the activated ensemble, we observed interesting

460 trade-offs between like-to-like amplification and suppression on different spatial scales. Such  
461 ensemble geometries are simply not possible in single-cell perturbation experiments. While  
462 another computational study (Cai et al., 2020) also examined the effects of stimulating a larger  
463 number of neurons, they only considered co-tuned ensembles and did not vary their spatial  
464 distribution.

465 Our combined *in vivo* and *in silico* interrogation of recurrent dynamics helps define an  
466 elementary logic for the impact of recurrent circuits on cortical activity. Our data and analysis  
467 demonstrate that recurrent activity does not simply amplify or suppress activity. Rather, the  
468 impact of recurrent circuits in L2/3 of mouse V1 depends jointly on physical space and feature  
469 space, both from the perspective of the activated ensemble and the other neurons in the  
470 network. Our computational modeling points to clear and testable predictions for the  
471 underlying circuitry that would support these local computations, which may be borne out in  
472 future experiments. The richness in recurrent modulation we discovered here might  
473 conceivably be suited to matching the sophisticated demands on the processing of complex  
474 images, such as occur naturally in the world. More generally, these principles our work reveals  
475 may constitute an elemental neural syntax of cortical transformations by recurrent circuits.

## 476 **Methods**

477 All experiments were performed in accordance with the guidelines and regulations of the ACUC  
478 of the University of California, Berkeley. Protocol #AUP-2014-10-6832-2.

### 479 *Mice*

480 All calcium imaging experiments were performed in mice of both sexes expressing GCaMP6s in  
481 excitatory neurons via tetO-GCaMP6s (Jax #024742) x Camk2a-tTA (Jax #003010). We  
482 confirmed the selectivity of this approach using RNAscope (SFig. 8). ChroME (Mardinly et al.,  
483 2018) or ChroME2s (Sridharan et al., 2022) was transfected via AAV. All constructs were  
484 bicistronically linked to a nuclear localized mRuby3 used for targeting photostimulation.  
485 Excitatory specificity was ensured using either a cre dependent AAV (Syn-ChroME Addgene  
486 170161; or CAG-ChroME2s Addgene 170163) in an excitatory specific cre line (Emx1-Cre, Jax  
487 #005628. Or SepW1-Cre MGI:5519915) or a Tta dependent AAV (Tre-ChroME or Tre-ChroME2s  
488 Addgene 170177) using the same Camk2-tTA source as above. In some cases, other cre lines  
489 (Jax #017320, or Jax #013044) were crossed to the tetO-GCaMP6s x Camk2-tTA line, with other  
490 cre dependent AAV fluorophores/indicators, those results are not a part of this study. No  
491 difference was observed between any mouse preparation (SFig. 9). Control mice had the same  
492 tetO-GCaMP6s x Camk2a-tTA without any viral injections. Mice were housed in cohorts of five  
493 or fewer in a reverse light:dark cycle of 12:12 hours, with experiments occurring during the dark  
494 phase.

### 495 *Surgery*

496 All experiments were performed in accordance with the guidelines and regulations of the  
497 Animal Care and Use Committee of the University of California, Berkeley. For head fixation  
498 during experiments, a small custom stainless-steel headplate was surgically implanted. Briefly,

499 adult mice (P35-P50) were anesthetized with 2-3% isoflurane and mounted in a stereotaxic  
500 apparatus. Body temperature was monitored and maintained at 37°C. The scalp was removed,  
501 the fascia retracted, and the skull lightly scored with a drill bit. Vetbond was applied to the skull  
502 surface, and the headplate was fixed to the skull with dental cement (Metabond). A fine-point  
503 marker was used to note the approximate location of bregma and the left primary visual cortex  
504 (V1; 2.7mm lateral, 0mm posterior to lambda). 2-3 burr holes were drilled using a dental drill  
505 (Foredom) with a 0.24mm drill bit (George Tiemann & Co.), and 200-300nl of AAV was injected  
506 at 50nl/min, followed by a 5+ min waiting period. A 3-3.5mm region of skull surrounding the  
507 marked V1 area was removed using the dental drill and/or a biopsy punch (Robbins  
508 Instruments). The window was replaced with three glass coverslips (two 3mm and one 5mm)  
509 and cemented into place with dental cement. Mice were given additional saline during surgery  
510 (0.3ml 0.9% NaCl). Mice received buprenorphine and meloxicam for pain management and  
511 dexamethasone to reduce brain swelling.

### 512 *Multiphoton Imaging and Stimulation Microscope*

513 All *in vivo* experiments were performed using a setup capable of 3D scanless holographic  
514 optogenetics with temporal focusing (3D-SHOT), as described previously (Pégard et al., 2017;  
515 Mardinly et al., 2018; Bounds et al., 2022; Sridharan et al., 2022). The microscope is adapted on  
516 a Movable Objective Microscope (MOM; Sutter Instrument Co.) platform, with three combined  
517 optical paths: a 3D two-photon (2P) photostimulation path, a fast resonant-galvo raster  
518 scanning 2P imaging path, and a widefield one-photon (1p) epifluorescence/IR-transmitted  
519 imaging path, merged by a polarizing beamsplitter before the microscope tube lens and  
520 objective. Imaging was performed with a Chameleon Ultra ii (Coherent inc), and  
521 photostimulation with a Monaco40 (Coherent inc). Temporal focusing of the photostimulation  
522 beam from the femtosecond fiber laser was achieved with a blazed holographic diffraction  
523 grating (R5000626767-19311 Newport Corporation). The beam was relayed through a rotating  
524 diffuser to randomize the phase pattern and expand the temporally focused beam to cover the  
525 area of the high-refresh-rate spatial light modulator (SLM; HSP1920-1064-HSP8-HB, 1920 ×  
526 1152 pixels, Meadowlark Optics). Holographic phase masks were calculated using the  
527 Gerchberg-Saxton algorithm and displayed on the SLM to generate multiple temporally-focused  
528 spots in 2D or 3D positions of interest. The photostimulation path was then relayed into the  
529 imaging path with a polarizing beamsplitter placed immediately prior to the tube lens. As  
530 described in Mardinly et al., 2018, to limit imaging artifacts introduced by the photostimulation  
531 laser, the photostimulation laser was synchronized to the scan phase of the resonance galvos  
532 using an Arduino Mega (Arduino), gated to be only on the edges of every line scan.

### 533 *Calibration*

534 Multiphoton activation of cells requires very precise alignment of the stimulation and the  
535 imaging system throughout a large 3D volume. Most calibration procedures assume that  
536 individual imaging and stimulation planes are parallel and flat. However, certain optical  
537 elements and subtle misalignments of the microscope can add aberrations that introduce  
538 mistargeting errors, especially at the edges of the field of view. For this reason, we improved  
539 our previous calibration approaches (Pégard et al., 2017; Mardinly et al., 2018; Oldenburg et al.,  
540 2022) with a new fully automated multiplexed 3D calibration, that accounts for arbitrary

541 distortions in either the imaging or stimulation planes (SFig. 1A-H). We confirmed that our  
542 system is able to deliver arbitrary powers to arbitrary locations in single and multi-target  
543 holograms. As expected, we found that multitarget holograms were less efficient than single  
544 target holograms, i.e., more light is lost to diffraction. But for holograms of 3 or more targets  
545 the light intensity hitting a given target is not affected by the identity or number of other  
546 targets (SFig. 1I). For this reason, in all subsequent experiments we restrict holograms to  
547 contain at least 3 target cells.

#### 548 *Holographic stimulation*

549 Cells were targeted for stimulation based on the nuclear localized mRuby signal bictronically  
550 linked to the opsin. Only multitarget holograms of at least 3 targets were used. Putative opsin  
551 positive cells were analyzed online using scanImage (vidrio inc) by collecting fluorescent scores  
552 around each automatically detected red nuclei. ROIs that were not holographically activatable  
553 were not included in further experiments. Online data was only used during the experiment  
554 and was not used in analyses.

555 To minimize the risk of off target activation, we minimize the power used per cell by first  
556 performing a ‘power test’ on each cell. In groups of 5 cells at a time, we activated each cell with  
557 five 5 ms pulses of light at powers ranging from 12.5 to 100 mW/cell. We define the stimable  
558 power as the power in which we could elicit a significant calcium response in a given cell.  
559 ChroME, and its derivatives, are useful in that using excess power does not easily elicit more  
560 than one spike per 5ms pulse (Mardinly et al., 2018; Bounds et al., 2022; Sridharan et al., 2022).  
561 Therefore, we multiply the stimable power by 1.1 to 1.2 to ensure more faithful response in  
562 each stimulated cell. Throughout the experiments, multi target holograms are designed such  
563 that each cell receives a distinct power based on its stimability and the diffraction efficiencies  
564 of each spot. We further restrict analysis to exclude cells within 15  $\mu\text{m}$  on the same plane or  
565 within 30  $\mu\text{m}$  one plane away (30  $\mu\text{m}$  spacing), as they have a risk of receiving off target light.

566 To confirm our resolution, we obtained physiological point spread functions in two separate  
567 experiments from a total of 26 matched cells. After the standard ‘power test’, randomly  
568 selected sets of 10 cells distributed throughout the field of view were driven as in a standard  
569 experiment. Holograms were digitally offset radially using 3  $\mu\text{m}$  steps (range -3 to 30  $\mu\text{m}$  from  
570 aligned), and axially in 6  $\mu\text{m}$  steps (range -6 to 60  $\mu\text{m}$ ). Resulting fluorescence was fit with a  
571 gaussian, aligned to the peak and the full width half max (FWHM) was obtained.

#### 572 *Calcium Imaging*

573 All recordings were performed in L2/3 imaging three 800 x 800  $\mu\text{m}$  planes, spaced 30 $\mu\text{m}$  apart,  
574 at 5.2-6.2Hz with <75mW 920nm laser light (Coherent Chameleon) using a resonant galvo  
575 system. Images were acquired using ScanImage (Vidrio Inc.) with custom stimulation control  
576 software. During recordings, animals are on a running wheel and their run speed is recorded.

577 Visual stimuli were presented on a 2048 x 1536 Retina iPad LCD display (Adafruit Industries)  
578 placed 10 cm from the mouse. The monitor backlight was synchronized with the galvos such  
579 that it came on only during the turnaround time, so that light from the monitor did not  
580 contaminate 2P imaging. Visual stimuli were created and presented with custom MATLAB code

581 and Psychophysics ToolBox. Drifting gratings (50 visual degrees, 1 Hz, .08 cycles per degree,  
582 100% contrast) of different orientations were randomly presented for 1 second each trial and  
583 interleaved with a grey-screen (“blank”) condition. Neurons with significantly different  
584 responses to visual stimuli ( $p < 0.05$ , ANOVA) were considered as visually responsive.

### 585 *Online Analysis*

586 Tuning curves and responses to photostimulation were calculated during the experiment, using  
587 a custom online implantation of CalmAn OnACID (Giovannucci et al., 2019) to perform rigid  
588 motion correction and seeded source extraction (<https://github.com/willyh101/live2p>).  
589 Preferred orientation (PO) was calculated as the max mean response to oriented gratings, and  
590 orientation selectivity was calculated as  $(PO-OO)/(PO+OO)$ .

### 591 *Discrete Optimizer*

592 In some experiments it was difficult to manually identify the optimal targets to create distinct  
593 ensembles that fit certain criteria, such as close and o-tuned ensembles. To overcome this  
594 challenge, we wrote a custom discrete optimizer. This optimizer selects groups of targets to  
595 stimulate from a database of eligible cells to minimize a custom cost function. As ‘cells to  
596 include’ is a discrete operation each step of our optimizer swaps one or more cells before  
597 evaluating the cost function and continuing. For a given experimental day we optimized for 3-  
598 20 ensemble of 10 cells that (1) were maximally distinct from each other, (2) minimized the  
599 number of times individual cells were included in different holograms, (3) prioritized cells  
600 activated with low light powers, (4) prioritized visually responsive cells, (5) avoided instances  
601 where two cells in the same ensemble were within 30  $\mu\text{m}$  of each other, (6) spread out cells  
602 within an ensemble, (7) fit the desired spatial rules (e.g. were spatially compact vs spread out),  
603 (8) fit the desired ensemble tuning (i.e. ensemble OSI), and (9) fit the desired mean selectivity  
604 (i.e., OSI of ensemble members was high for co-tuned ensembles or low for untuned  
605 ensembles).

### 606 *Offline Analysis*

607 Tiff files were motion corrected, cell sources (aka pixel masks) were determined, and source  
608 fluorescence was extracted using suite2p (Pachitariu et al., 2017). Pixel masks were manually  
609 categorized as ‘cells’ or ‘not cells’ and only ‘cells’ were included for analysis. For  $\Delta F/F$   
610 calculation, each cell’s detected fluorescence was first neuropil subtracted. The average  
611 fluorescence of an annulus (not containing another cell) of up to 350 pixels was considered  
612 neuropil. A neuropil coefficient ( $c$ ) was calculated for each cell as described in (Pachitariu et al.,  
613 2017) and the final fluorescence was calculated as  $F = F_{\text{cell}} - c * F_{\text{neuropil}}$ .  $F_0$ , the ‘baseline’  
614 fluorescence, was calculated with a moving average of the 10<sup>th</sup> percentile of a 1000 frame  
615 window (approx. 3 minute); this moving average corrected for very slow drift in imaging  
616 conditions.  $\Delta F/F$  is  $(F - F_0)/F_0$ .

617 Not all putative cells identified via red nuclei and/or online analysis were recovered by suite2p.  
618 This ‘non-matched’ population could be caused by a variety of sources, including errors in the  
619 online initial detection algorithms, errors in suite2p’s recovery, and potentially errors in the  
620 manual ‘cell’ vs ‘not cell’ determination. If too many cells of an ensemble did not match that

621 ensemble was excluded (see exclusions). When calculating distance to a target, or spread of an  
622 ensemble, the targeted rather than recovered sets of coordinates are used.

623 The minimum distance to a target was defined for each cell as the minimum distance to any  
624 attempted target, regardless of if that target 'matched' to a suite2p detected cell.

625 The spread of an ensemble was calculated as the mean pairwise distance between the center of  
626 mass of each target of an ensemble calculated in 3D. A close ensemble is defined as having a  
627 mean pairwise distance  $< 200 \mu\text{m}$  whereas a far apart ensemble has a mean distance  $> 200 \mu\text{m}$ .

628 Tuning curves and OSIs were recalculated offline data for subsequent analysis. Ensemble OSI is  
629 defined as the OSI of the mean tuning curve from cells used in an ensemble. Mean OSI is the  
630 arithmetic mean of the OSIs from each ensemble. Co-Tuned ensembles are defined as  
631 ensembles with an ensemble OSI  $> 0.7$  and a mean OSI  $> 0.5$ ; untuned ensembles are defined as  
632 ensembles with an ensemble OSI  $< 0.3$  and a mean OSI  $< 0.5$ .

### 633 *Exclusion Criteria*

634 Trials were excluded if (1) the animal ran more than 6 cm/s, (2) 50% or more of the targeted  
635 cells failed to respond when driven (to at least 0.25 Z-scored Fluorescence above baseline), or  
636 (3) registration of the field of view indicates that the brain shifted more than  $4.7 \mu\text{m}$  (3 pixels),  
637 indicating a miss.

638 Cells were excluded from a given trial if (1) they were located in an off target region ( $15 \mu\text{m}$   
639 radially from a targeted cell, or  $30 \mu\text{m}$  radially from a cell one plane away), (2) they had been  
640 stimulated in the immediate preceding trial, (3) they were occluded by the stimulation artifact,  
641 or (4) the cell was categorized as 'not cell' or not detected via the suite2p process.

642 Ensembles were excluded from analysis if (1) more than 33% of the targeted cells were not  
643 detected via suite2p, (2) more than 50% of attempted stimulation trials failed (note only  
644 successful trials are included), or had fewer than 10 repetitions for either the baseline (4) or  
645 stimulation (5) conditions.

646 Fields of view were excluded from analysis if (1) fewer than 5% of cells were visually responsive,  
647 (2) more than 50% of trials were occurred while the mouse was running, or (3) fewer than 250  
648 total cells were detected by suite2p.

### 649 *Determining Opsin Negative Cells*

650 Opsin positive and opsin negative cells were identified in SepW1-Cre x CamK2a-tTA x tetO-  
651 GCaMP6s mice injected with AAV-CAG-DIO-ChroME2s-P2A-H2B-mRuby3 as described above. In  
652 addition to the typical imaging procedures, a structural image of the field of view at 1020nm  
653 was taken at the start of an experiment to identify and quantify the brightness of the nuclear  
654 mRuby3. As window preparations and imaging conditions could vary between days the mRuby3  
655 brightness was considered a relative measure. For each field of view the top 20% brightest red  
656 nuclei were defined as opsin positive, while the 30% dimmest were considered opsin negative.  
657 Opsin negative cells often scored low integer values fluorescent counts, with many cells  
658 receiving equal scores, thus in some recordings more than 30% of cells were included.

659 *Mathematical model*

660 We consider a two-dimensional neural field model of the form

$$661 \quad \tau_{\alpha} \frac{\partial r_{\alpha}}{\partial t} = -r_{\alpha} + \phi_{\alpha}(j_{\alpha e} * r_e + j_{\alpha i} * r_i + \mu_{\alpha}),$$

662 where \* denotes a two-dimensional convolution in space,  $\alpha = e, i$ , and  $x \in [0,1400] \times$   
 663  $[0,1400]\mu\text{m}$  box with periodic boundary conditions (modified from Huang et al., 2019). Since  
 664 the animal is viewing a gray screen, there exists a uniform steady state for this system  $\mathbf{r}_{ss}$ . We  
 665 then make use of the fact that the perturbation to the system is relatively weak, and as a result,  
 666 we can approximate it as a linear perturbation around  $\mathbf{r}_{ss}$ . Linearizing the system yields

$$667 \quad T \frac{\partial \Delta \mathbf{r}}{\partial t} = (-I + W) * \Delta \mathbf{r},$$

668 where

$$669 \quad W_{\alpha\beta} = g_{\alpha} \cdot j_{\alpha\beta}$$

670 with  $g_{\alpha}$  being the gain set by the steady state of the system. The optogenetic stimulation is  
 671 then modeled by considering

$$672 \quad T \frac{\partial \Delta \mathbf{r}}{\partial t} = (-I + W) * (\Delta \mathbf{r} + r_{stim})$$

673 where  $r_{stim} = 10 \cdot \delta(x - x_i)\delta(y - y_i)$  at ten stim locations denoted by  $(x_i, y_i)$ . Transforming  
 674 the system into Fourier space, we can solve for  $\Delta \mathbf{r}$  in steady state

$$675 \quad \Delta \tilde{\mathbf{r}} = (I - \tilde{W})^{-1} \cdot \tilde{W} \cdot \tilde{r}_{stim}$$

676 We can perform a matrix expansion of this inverse as long as the spectral radius of  $\tilde{W}$  is less  
 677 than one. Since V1 is in a low gain state while the animal is viewing a gray screen, the effective  
 678 connection strength is very weak (i.e.,  $g_{\alpha} \ll 1$ ), placing us within this regime. Performing this  
 679 expansion yields

$$680 \quad \Delta \tilde{\mathbf{r}} = (I + \tilde{W} + \tilde{W}^2 + \dots) \cdot \tilde{W} \cdot \tilde{r}_{stim}.$$

681 Finally, after taking the inverse Fourier transform, we find that

$$682 \quad \Delta \mathbf{r} = (W + W * W + W^{*3} + \dots) * r_{stim},$$

$$683 \quad \Delta \mathbf{r} \approx (W + W * W) * r_{stim}$$

684 where we again made use of the weak effective connectivity to drop the higher ordered terms.  
 685 Since we are only stimulating and recording from excitatory neurons, we can write this  
 686 approximation as a sum of monosynaptic and disynaptic excitatory terms, and a disynaptic  
 687 inhibitory pathway

$$688 \quad \Delta r_e \approx (W_{ee} + W_{ee} * W_{ee}) * r_{stim} + W_{ei} * W_{ie} * r_{stim}.$$

689 While we consider connectivity rules that depend on both space and feature, we assume that  
 690 these components are independent. This allows us to write the strength of connection between  
 691 neurons at coordinates  $(x_1, y_1)$  and  $(x_2, y_2)$  with feature preference  $\theta_1$  and  $\theta_2$ , respectively, as

$$692 \quad W_{\alpha\beta}(x_1, y_1, \theta_1; x_2, y_2, \theta_2) = w_{\alpha\beta} \cdot g_{\beta}(x_1 - x_2; \sigma_{\beta}) \cdot g_{\beta}(y_1 - y_2; \sigma_{\beta}) \cdot h_{\beta}(\theta_1 - \theta_2) / Z$$

693 where  $Z$  is a normalization factor to ensure that the integral of  $W_{\alpha\beta}$  equals  $w_{\alpha\beta}$ . The spatial  
 694 dependence is given by the following sum of wrapped Gaussian distributions

$$695 \quad g_{\alpha}(x; \sigma_{\alpha}) = \frac{(1 - \kappa_{\alpha})}{\sqrt{2\pi}\sigma_{\alpha,b}} \cdot \sum_{k=-\infty}^{\infty} e^{-(x+k)^2/(2\sigma_{\alpha,b}^2)} + \frac{\kappa_{\alpha}}{\sqrt{2\pi}\sigma_{\alpha,n}} \cdot \sum_{k=-\infty}^{\infty} e^{-(x+k)^2/(2\sigma_{\alpha,n}^2)}$$

696 where  $\sigma_{\alpha,b}$  refers to the broad spatial component,  $\sigma_{\alpha,n}$  is the narrow spatial component, and  $\kappa_{\alpha}$   
 697 is the relative weight of each of them. The broad spatial components for both outgoing  
 698 excitatory and inhibitory connections are fit according to data from (Rossi et al., 2020) (SFig. 5A-  
 699 D). The parameters of the narrow component,  $\sigma_{\alpha,n}$  and  $\kappa_{\alpha}$ , are adjusted from Yu et al. (2020),  
 700 chosen to capture the nearby excitation observed in Fig. 2A and SFig. 5E. Further, the boundary  
 701 of the experimentally observed data regime box used in Fig. 2C was found by fitting  
 702 experimental data for different bin widths (5  $\mu$ m-20  $\mu$ m) to the function

$$703 \quad f(d) = A_1 e^{(d/\sigma_1)^2} + A_2 e^{(d/\sigma_2)^2},$$

704 solving for the zero crossing and max activation/max suppression, and then taking the  
 705 boundary to be the smallest rectangle that includes the values for all bin widths.

706 The models without feature-based connectivity take  $h_{\alpha}(\theta)$ . Otherwise, it takes the form

$$707 \quad h_{\alpha}(\theta) = r_0 + r_p \cdot e^{-\theta^2/(2\sigma_{\alpha\beta}^2)},$$

708 where  $\theta \in [0,90]$ . The parameters for feature-based excitatory connections are also fitted  
 709 according to data from (Rossi et al., 2020), whereas the inhibitory connections are adjusted to  
 710 best match the observed like-to-like suppression seen in Fig. 4. After using the available data,  
 711 the free parameters are the effective strength of excitatory connections,  $w_{ee}$ , the effective  
 712 strength of the inhibitory pathway,  $w_{eie} = w_{ei} \cdot w_{ie}$ , the narrow spatial components  
 713 parameters, and the feature base rules of the inhibitory connections.

#### 714 *RNA in situ hybridization*

715 Brain was harvested from a 6 months old tetO-GCaMP6s+/+ CamK2a-tTA+/- female, embedded  
 716 in optimal cutting temperature compound (OCT, Tissue-Tek), and frozen on dry ice within 5  
 717 minutes of tissue harvest. Tissue blocks were cut into 10  $\mu$ m sections using a cryostat.

718 RNAscope™ was performed on the sections according to the manufacturer's instructions  
 719 (RNAscope™ Fluorescent Multiplex Kit, Advanced Cell Diagnostics). Probes used were Mm-  
 720 GCaMP6s-O1, Mm-Slc32a1-C2, and Mm-Slc17a7-C3. RTU DAPI was used to stain cell nuclei and  
 721 slides were mounted using Vectashield mounting medium (Vector Labs). Images were collected  
 722 using LSM 880 NLO AxioExaminer confocal microscope (Zeiss) and processed using ZEN lite  
 723 (Zeiss). For analysis, 300 cells with positive DAPI staining were counted in cortical Layer 2/3 and

724 positive/negative staining of each probe was recorded for each cell. Cell with less than 10 dots  
725 per probe was presumed negative for the respective RNA.

#### 726 *Data/Model Availability*

727 The data and code will be made available upon acceptance for publication.

#### 728 *Acknowledgements*

729 This work was supported by NIH grants U19NS107613, R01EY023756, RF1MH120680,  
730 UF1NS107574 and a New York Stem Cell Robertson Fellowship and Chan Zuckerberg Biohub  
731 Investigator Award to H.A.; NIH grants U19NS107613 and R01EB026953, and a grant from the  
732 Simons foundation collaboration on the global brain to B.D.; NSF Fellowship DGE 1752814 to  
733 H.A.B; Swartz Foundation Fellowship for Theory in Neuroscience, and the Burroughs Wellcome  
734 Fund's Career Award at the Scientific Interface to G.H.; NIH Grant F31EY031977 to W.D.H.; and  
735 NIH grant K99EY029758 and the Simons Foundation collaboration on the global brain fellowship  
736 to I.A.O.

737

738

#### 739 **References**

740 Adesnik H, Bruns W, Taniguchi H, Huang ZJ, Scanziani M (2012) A neural circuit for spatial  
741 summation in visual cortex. *Nature* 490:226–231.

742 Anderson JS, Carandini M, Ferster D (2000) Orientation Tuning of Input Conductance,  
743 Excitation, and Inhibition in Cat Primary Visual Cortex. *Journal of Neurophysiology*  
744 84:909–926.

745 Billeh YN, Cai B, Gratiy SL, Dai K, Iyer R, Gouwens NW, Abbasi-Asl R, Jia X, Siegle JH, Olsen SR,  
746 Koch C, Mihalas S, Arkhipov A (2020) Systematic Integration of Structural and Functional  
747 Data into Multi-scale Models of Mouse Primary Visual Cortex. *Neuron* 106:388-403.e18.

748 Bonin V, Histed MH, Yurgenson S, Reid RC (2011) Local Diversity and Fine-Scale Organization of  
749 Receptive Fields in Mouse Visual Cortex. *J Neurosci* 31:18506–18521.

750 Bounds HA, Sadahiro M, Hendricks WD, Gajowa M, Gopakumar K, Quintana D, Tasic B, Daigle  
751 TL, Zeng H, Oldenburg IA, Adesnik H (2022) Ultra-precise all-optical manipulation of  
752 neural circuits with multifunctional Cre-dependent transgenic mice. :2021.10.05.463223  
753 Available at: <https://www.biorxiv.org/content/10.1101/2021.10.05.463223v3> [Accessed  
754 August 8, 2022].

755 Cai B, Billeh YN, Chettih SN, Harvey C, Koch C, Arkhipov A, Mihalas S (2020) Modeling robust  
756 and efficient coding in the mouse primary visual cortex using computational  
757 perturbations. *bioRxiv*:2020.04.21.051268.

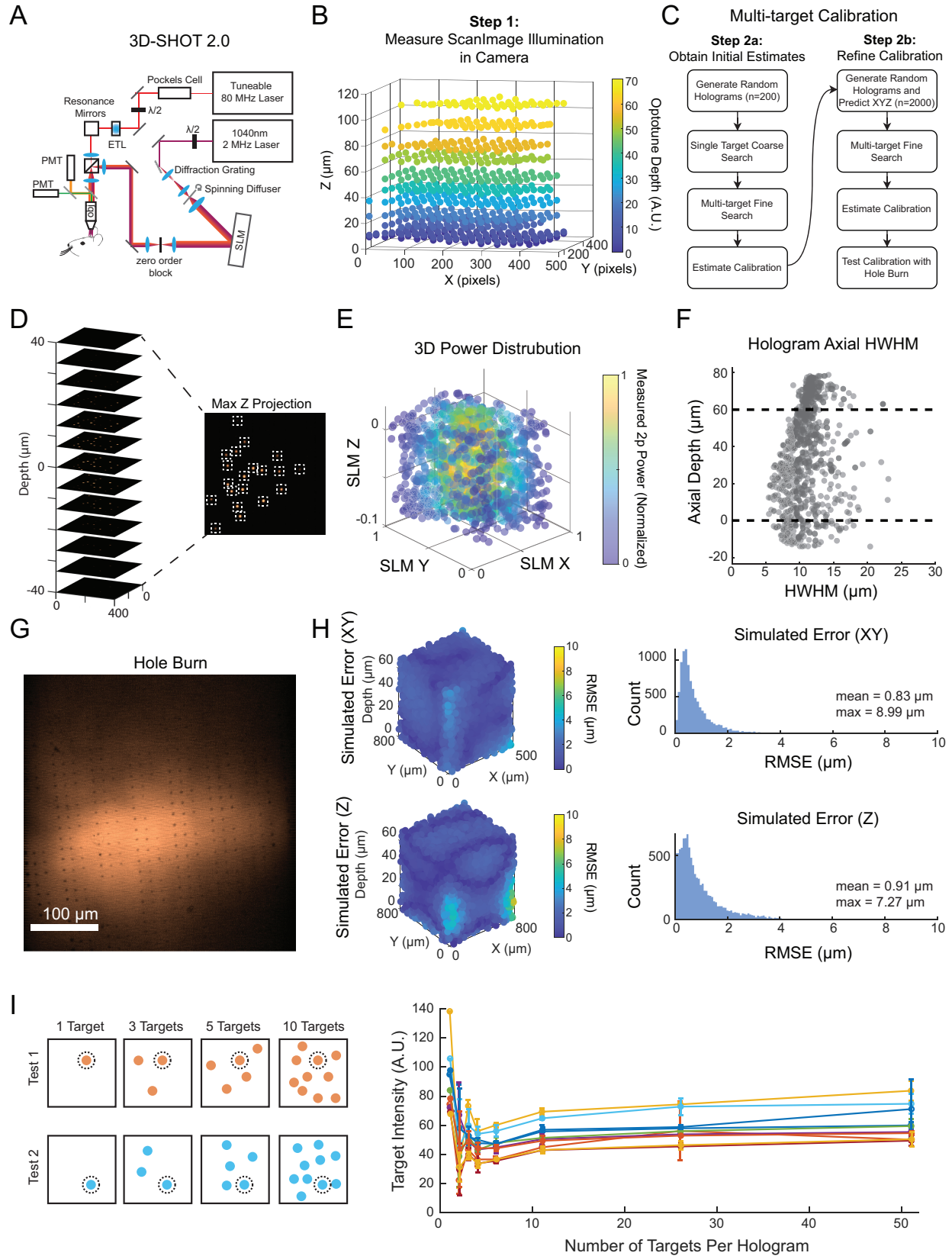
758 Campagnola L et al. (2022) Local connectivity and synaptic dynamics in mouse and human  
759 neocortex. *Science* 375.

- 760 Carrillo-Reid L, Yang W, Bando Y, Peterka DS, Yuste R (2016) Imprinting and recalling cortical  
761 ensembles. *Science* 353:691–694.
- 762 Cavanaugh JR, Bair W, Movshon JA (2002) Nature and Interaction of Signals From the Receptive  
763 Field Center and Surround in Macaque V1 Neurons. *Journal of Neurophysiology*  
764 88:2530–2546.
- 765 Chettih SN, Harvey CD (2019) Single-neuron perturbations reveal feature-specific competition  
766 in V1. *Nature* 567:334–340.
- 767 Cossell L, Iacaruso MF, Muir DR, Houlton R, Sader EN, Ko H, Hofer SB, Mrsic-Flogel TD (2015)  
768 Functional organization of excitatory synaptic strength in primary visual cortex. *Nature*  
769 518:399–403.
- 770 Dalgleish HW, Russell LE, Packer AM, Roth A, Gauld OM, Greenstreet F, Thompson EJ, Häusser  
771 M (2020) How many neurons are sufficient for perception of cortical activity? Bathellier  
772 B, Calabrese RL, Bathellier B, Carrillo-Reid L, eds. *eLife* 9:e58889.
- 773 Derdikman D, Hildesheim R, Ahissar E, Arieli A, Grinvald A (2003) Imaging Spatiotemporal  
774 Dynamics of Surround Inhibition in the Barrels Somatosensory Cortex. *J Neurosci*  
775 23:3100–3105.
- 776 Douglas RJ, Koch C, Mahowald M, Martin KAC, Suarez HH (1995) Recurrent Excitation in  
777 Neocortical Circuits. *Science* 269:981–985.
- 778 Dräger UC (1975) Receptive fields of single cells and topography in mouse visual cortex. *Journal*  
779 *of Comparative Neurology* 160:269–289.
- 780 Ferster D, Chung S, Wheat H (1996) Orientation selectivity of thalamic input to simple cells of  
781 cat visual cortex. *Nature* 380:249–252.
- 782 Garrett ME, Nauhaus I, Marshel JH, Callaway EM (2014) Topography and Areal Organization of  
783 Mouse Visual Cortex. *Journal of Neuroscience* 34:12587–12600.
- 784 Giovannucci A, Friedrich J, Gunn P, Kalfon J, Brown BL, Koay SA, Taxidis J, Najafi F, Gauthier JL,  
785 Zhou P, Khakh BS, Tank DW, Chklovskii DB, Pnevmatikakis EA (2019) CalmAn an open  
786 source tool for scalable calcium imaging data analysis Kleinfeld D, King AJ, eds. *eLife*  
787 8:e38173.
- 788 Gómez-Laberge C, Smolyanskaya A, Nassi JJ, Kreiman G, Born RT (2016) Bottom-Up and Top-  
789 Down Input Augment the Variability of Cortical Neurons. *Neuron* 91:540–547.
- 790 Hage TA, Bosma-Moody A, Baker CA, Kratz MB, Campagnola L, Jarsky T, Zeng H, Murphy GJ  
791 (2022) Synaptic connectivity to L2/3 of primary visual cortex measured by two-photon  
792 optogenetic stimulation. *eLife* 11:e71103.

- 793 Holmgren C, Harkany T, Svennenfors B, Zilberter Y (2003) Pyramidal cell communication within  
794 local networks in layer 2/3 of rat neocortex. *The Journal of Physiology* 551:139–153.
- 795 Huang C, Ruff DA, Pyle R, Rosenbaum R, Cohen MR, Doiron B (2019) Circuit Models of Low-  
796 Dimensional Shared Variability in Cortical Networks. *Neuron* 101:337-348.e4.
- 797 Ichida JM, Schwabe L, Bressloff PC, Angelucci A (2007) Response Facilitation From the  
798 “Suppressive” Receptive Field Surround of Macaque V1 Neurons. *Journal of*  
799 *Neurophysiology* 98:2168–2181.
- 800 Isaacson JS, Scanziani M (2011) How Inhibition Shapes Cortical Activity. *Neuron* 72:231–243.
- 801 Kang K, Shelley M, Sompolinsky H (2003) Mexican hats and pinwheels in visual cortex. *Proc Natl*  
802 *Acad Sci USA* 100:2848–2853.
- 803 Kapfer C, Glickfeld LL, Atallah BV, Scanziani M (2007) Supralinear increase of recurrent  
804 inhibition during sparse activity in the somatosensory cortex. *Nature Neuroscience*  
805 10:743–753.
- 806 Ko H, Cossell L, Baragli C, Antolik J, Clopath C, Hofer SB, Mrsic-Flogel TD (2013) The emergence  
807 of functional microcircuits in visual cortex. *Nature* 496:96–100.
- 808 Ko H, Hofer SB, Pichler B, Buchanan KA, Sjöström PJ, Mrsic-Flogel TD (2011) Functional  
809 specificity of local synaptic connections in neocortical networks. *Nature* 473:87–91.
- 810 Kondo S, Yoshida T, Ohki K (2016) Mixed functional microarchitectures for orientation  
811 selectivity in the mouse primary visual cortex. *Nat Commun* 7:13210.
- 812 Kwan AC, Dan Y (2012) Dissection of Cortical Microcircuits by Single-Neuron Stimulation In Vivo.  
813 *Current Biology* 22:1459–1467.
- 814 Lee W-CA, Bonin V, Reed M, Graham BJ, Hood G, Glattfelder K, Reid RC (2016) Anatomy and  
815 function of an excitatory network in the visual cortex. *Nature* 532:370–374.
- 816 Levy RB, Reyes AD (2012) Spatial profile of excitatory and inhibitory synaptic connectivity in  
817 mouse primary auditory cortex. *Journal of Neuroscience* 32:5609–5619.
- 818 Li L, Li Y, Zhou M, Tao HW, Zhang LI (2013a) Intracortical multiplication of thalamocortical  
819 signals in mouse auditory cortex. *Nat Neurosci* 16:1179–1181.
- 820 Li Y, Ibrahim LA, Liu B, Zhang LI, Tao HW (2013b) Linear transformation of thalamocortical input  
821 by intracortical excitation. *nature NEUROSCIENCE* 16:9.
- 822 Lien AD, Scanziani M (2013) Tuned thalamic excitation is amplified by visual cortical circuits. *Nat*  
823 *Neurosci* 16:1315–1323.

- 824 Mardinly AR, Oldenburg IA, Pégard NC, Sridharan S, Lyall EH, Chesnov K, Brohawn SG, Waller L,  
825 Adesnik H (2018) Precise multimodal optical control of neural ensemble activity. *Nature*  
826 *Neuroscience* 21:881–893.
- 827 Marshel JH, Kim YS, Machado TA, Quirin S, Benson B, Kadmon J, Raja C, Chibukhchyan A,  
828 Ramakrishnan C, Inoue M, Shane JC, McKnight DJ, Yoshizawa S, Kato HE, Ganguli S,  
829 Deisseroth K (2019) Cortical layer–specific critical dynamics triggering perception.  
830 *Science* 365 Available at: <https://science.sciencemag.org/content/365/6453/eaaw5202>  
831 [Accessed February 2, 2021].
- 832 Mossing DP, Veit J, Palmigiano A, Miller KD, Adesnik H (2021) Antagonistic inhibitory  
833 subnetworks control cooperation and competition across cortical space. *Neuroscience*.  
834 Available at: <http://biorxiv.org/lookup/doi/10.1101/2021.03.31.437953> [Accessed July  
835 3, 2022].
- 836 Nassi JJ, Lomber SG, Born RT (2013) Corticocortical Feedback Contributes to Surround  
837 Suppression in V1 of the Alert Primate. *Journal of Neuroscience* 33:8504–8517.
- 838 Ocker GK, Hu Y, Buice MA, Doiron B, Josić K, Rosenbaum R, Shea-Brown E (2017) From the  
839 statistics of connectivity to the statistics of spike times in neuronal networks. *Current*  
840 *Opinion in Neurobiology* 46:109–119.
- 841 Ohki K, Chung S, Ch’ng YH, Kara P, Reid RC (2005) Functional imaging with cellular resolution  
842 reveals precise micro-architecture in visual cortex. *Nature* 433:597–603.
- 843 Ohki K, Reid RC (2007) Specificity and randomness in the visual cortex. *Curr Opin Neurobiol*  
844 17:401–407.
- 845 Oldenburg IA, Bounds HA, Pégard, NC (2022) Three-dimensional scanless holographic  
846 optogenetics with temporal focusing (3D-SHOT). In: *All-Optical Methods to Study Neural*  
847 *Function*. Humana Press.
- 848 Pachitariu M, Stringer C, Dipoppa M, Schröder S, Rossi LF, Dagleish H, Carandini M, Harris KD  
849 (2017) Suite2p: beyond 10,000 neurons with standard two-photon microscopy. :061507  
850 Available at: <https://www.biorxiv.org/content/10.1101/061507v2> [Accessed August 8,  
851 2022].
- 852 Pégard NC, Mardinly AR, Oldenburg IA, Sridharan S, Waller L, Adesnik H (2017) Three-  
853 dimensional scanless holographic optogenetics with temporal focusing (3D-SHOT).  
854 *Nature Communications* 8:1–14.
- 855 Reinhold K, Lien AD, Scanziani M (2015) Distinct recurrent versus afferent dynamics in cortical  
856 visual processing. *Nat Neurosci* 18:1789–1797.

- 857 Ringach DL, Mineault PJ, Tring E, Olivas ND, Garcia-Junco-Clemente P, Trachtenberg JT (2016)  
858 Spatial clustering of tuning in mouse primary visual cortex. *Nature Communications*  
859 7:12270.
- 860 Rossi LF, Harris KD, Carandini M (2020) Spatial connectivity matches direction selectivity in  
861 visual cortex. *Nature* 588:648–652.
- 862 Russell LE, Yang Z, Tan PL, Fişek M, Packer AM, Dalglish HWP, Chettih S, Harvey CD, Häusser M  
863 (2019) The influence of visual cortex on perception is modulated by behavioural state.  
864 bioRxiv:706010.
- 865 Sadeh S, Clopath C (2020) Theory of neuronal perturbome in cortical networks. *Proceedings of*  
866 *the National Academy of Sciences of the United States of America* 117:26966–26976.
- 867 Shushruth S, Mangapathy P, Ichida JM, Bressloff PC, Schwabe L, Angelucci A (2012) Strong  
868 Recurrent Networks Compute the Orientation Tuning of Surround Modulation in the  
869 Primate Primary Visual Cortex. *Journal of Neuroscience* 32:308–321.
- 870 Sridharan S, Gajowa MA, Ogando MB, Jagadisan UK, Abdeladim L, Sadahiro M, Bounds HA,  
871 Hendricks WD, Turney TS, Tayler I, Gopakumar K, Oldenburg IA, Brohawn SG, Adesnik H  
872 (2022) High-performance microbial opsins for spatially and temporally precise  
873 perturbations of large neuronal networks. *Neuron* 110:1139-1155.e6.
- 874 Wagor E, Mangini NJ, Pearlman AL (1980) Retinotopic organization of striate and extrastriate  
875 visual cortex in the mouse. *J Comp Neurol* 193:187–202.
- 876 Yu P, Yang Y, Dipoppa M, Rossi FL, Daisong P, Fan JL, Huang C, Miller KD, Ji N, Doiron BD (2020)  
877 Measuring and modeling a fine spatial scale clustering of orientation tuning in L2/3 of  
878 mouse V1. In: *Cosyne*. To be published.
- 879 Zhuang J, Ng L, Williams D, Valley M, Li Y, Garrett M, Waters J (2017) An extended retinotopic  
880 map of mouse cortex Kleinfeld D, ed. *eLife* 6:e18372.
- 881 Znamenskiy P, Kim MH, Muir DR, Iacaruso MF, Hofer SB, Mrsic-Flogel TD (2018) Functional  
882 selectivity and specific connectivity of inhibitory neurons in primary visual cortex.  
883 bioRxiv.
- 884
- 885
- 886
- 887
- 888
- 889



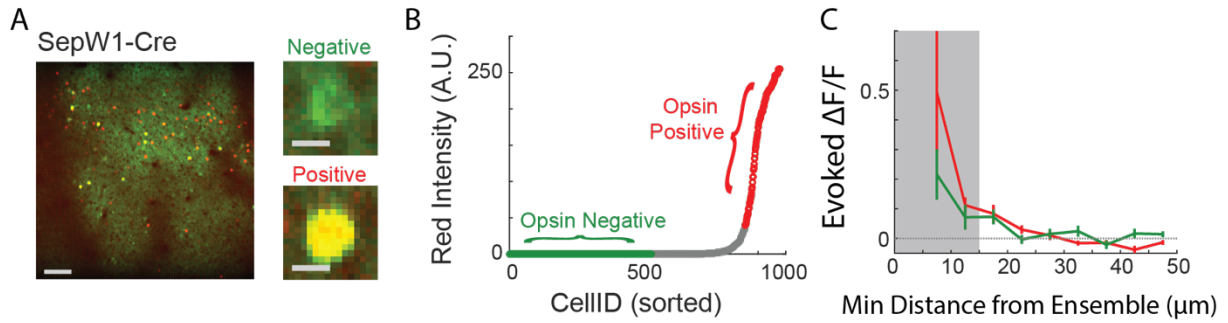
**SFig 1: 3D-SHOT2.0 and 3D spatial calibration.** **A:** Microscope setup implementing simultaneous holographic optogenetics (via 3D-SHOT 2.0) and 2-photon calcium imaging. Imaging and stimulation paths are co-aligned and calibrated using the procedure outlined in this figure. **B:** First, a substage camera is used to image the ‘imaging’ fields of view in three dimensions. A thin fluorescent slide is imaged by the camera, and the microscope focus moved above and below the slide to gain depth information. The field curvature, introduced by the ETL, among other elements, was measured as a function of XY position and depth and then fit with a polynomial. Multiple ETL offsets representing the different imaging planes that might be used in an experiment are imaged separately. **C:** Second, we devised a multiplexed approach to register the position and diffraction efficiency of hologram targets (aka individual illuminated spots) throughout the Imaging FOV. To begin, the approximate XYZ position of 200 randomly targeted single-target holograms were determined by imaging a with the substage camera. Each hologram was projected onto the thin film slide, and then a z-stack of images made by defocusing the microscope. The XY position of each hologram was determined by the position on the camera, while the Z position inferred from the stack. Next, multi-target holograms comprised of the holograms imaged in the initial phase were imaged at a higher resolution to provide a more accurate XYZ position. By imaging holograms as multi-targets we were able to parallelize data acquisition and dramatically improve calibration times. Next, we use the initial 200 imaged holograms to estimate the calibration and registration of holograms in the imaging FOV. Using these initial model fits, we then generate 100 20-target holograms (for a total of 2000 data points), predict their location in the substage camera, and extract the resulting XYZ position, relative power, and HWHM throughout the entire imaging FOV. Data were fit with a polynomial to generate a general transform for any SLM and imaging coordinate. Finally, we test the spatial calibration with an automated “hole-burn”. **D:** An example of a multi-target hologram being imaged in a stack. **E:** Example power distributions in 3D (presented in arbitrary SLM units). Power distributions vary significantly throughout 3D. By modeling hologram diffraction efficiency in 3D, we can dynamically compensate power during an experiment to accurately use a greater range of the SLM. Each point represents a single imaged hologram; color represents the relative power from that hologram. **F:** Axial hologram HWHM varies as a function of depth. We co-aligned the axial position of the imaging and holographic stimulation pathways such that the holograms with smallest HWHM were positioned within the typical Imaging axial range used in experiments (dashed lines). Each point represents a single imaged hologram. **G:** Example image from the automated “hole-burn”. A unique pattern is bleached/burned onto a thin fluorescent slide, imaged in ScanImage, and the XY position of hole-burn locations is detected. This process is repeated for multiple z-planes. **H:** With the calibration in place, we simulated XY (top) and Z (bottom) error in targeting throughout the typical imaging field of view (n=10,000 simulations). Root-mean-square error (RMSE, in  $\mu\text{m}$ ) is presented in 3D (left) and overall error distributions (right). **I:** To understand the variability in delivered power across different types of holograms, we measured the fluorescence evoked by a series of 10 test targets (dotted circle, left). Using the substage camera, we measured the intensity from the test target alone in a single-target hologram, or in a hologram that also contained 1 to 50 randomly chosen ‘distractor’ targets, 10 repeats with new distractor targets were performed per test target and hologram size. *Right*, the intensity of each test target as a function of the total number of targets in the hologram. Each color denotes a different test target, while the variability comes from different ‘distractor’ targets (presented as S.E.M).

891

892

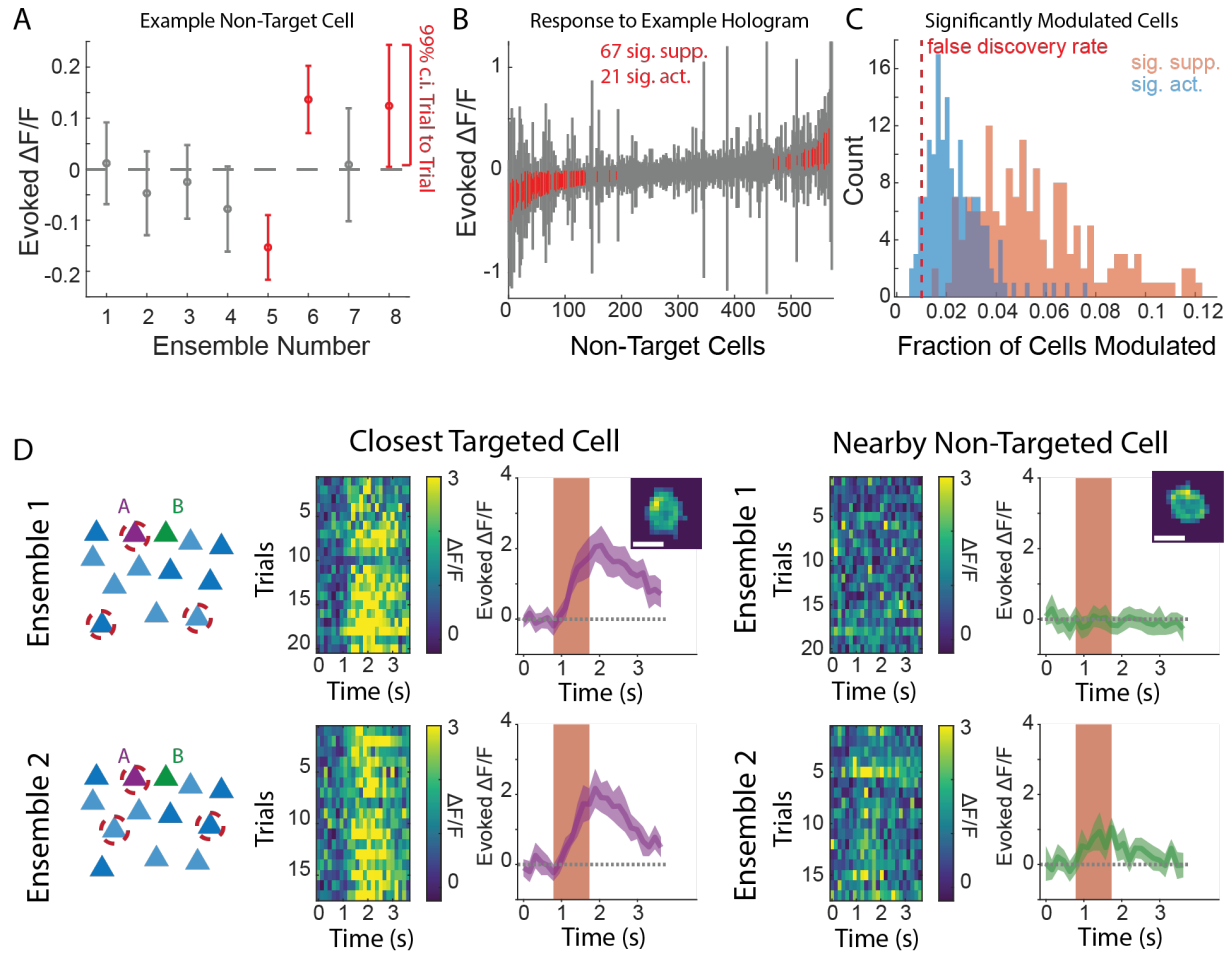
893

894

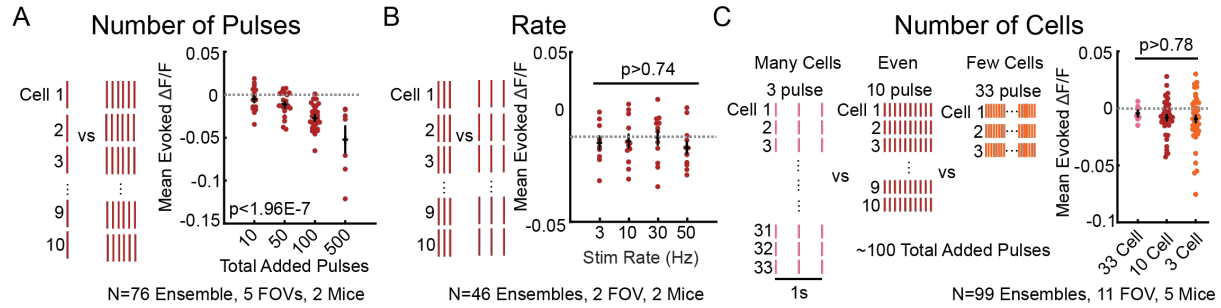


**SFig 2: Sparsely Expressing Mice for analysis of opsin negative cells.** **A:** Representative image from a FOV of a SepW1-Cre mouse with AAV CAG-DIO-ChroME2. Scale Bar 100  $\mu\text{m}$ . Inset, example images of opsin negative (above) and opsin positive (below) cell. Scale Bar (10  $\mu\text{m}$ ). Green is from GCaMP, red from nuclear localized mRuby3 part of the opsin construct. **B:** The intensity of the red fluorophore detected for each cell in a field of view. Top 80<sup>th</sup> percentile categorized as opsin positive, bottom 30<sup>th</sup> percentile opsin negative (Note: red counts are integers and more than 30% of cells may have the same or lower 30<sup>th</sup> percentile score). **C:** Evoked  $\Delta F/F$  responses in non-targeted cells to 10 cell ensemble stimulation as a function of distance from the closest target, separated by opsin positive and opsin negative cells. Exclusion zone (15  $\mu\text{m}$ ) marked in grey. N= 57 ensembles, 6 FOVs, 4 Mice.

895

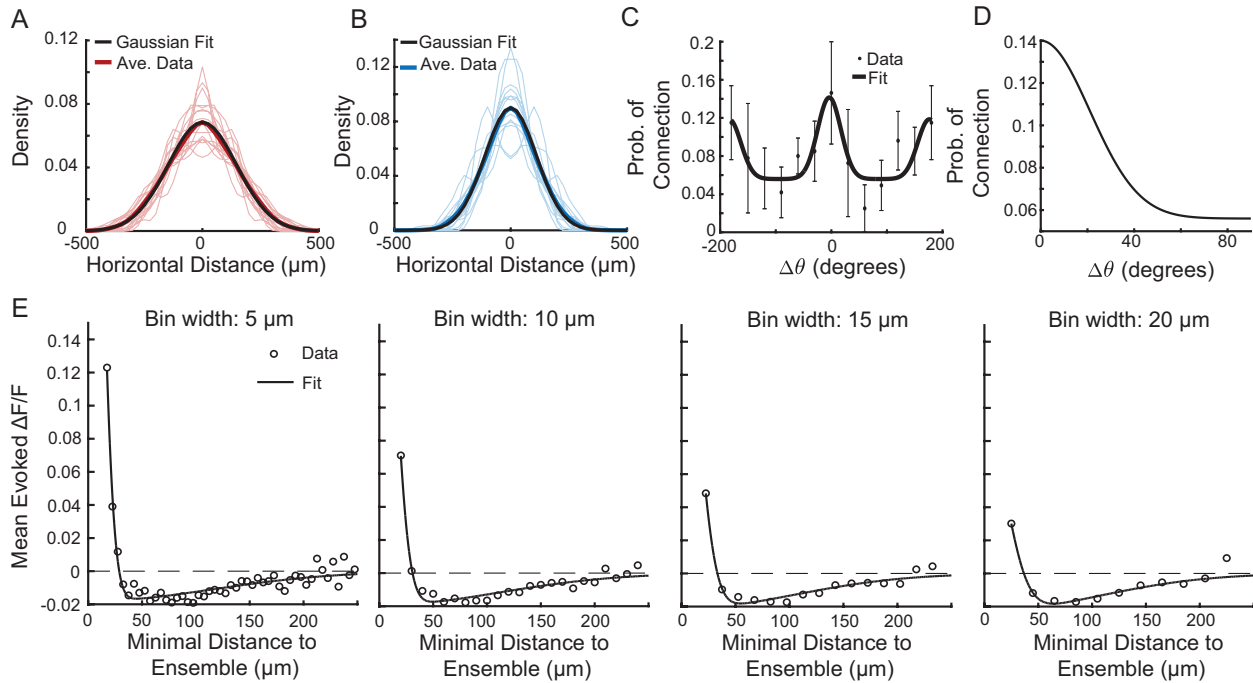


**SFig 3: Heterogeneity in Responses to Holographic Stimulation.** **A:** Evoked  $\Delta F/F$  responses in a single example non-target cell to 8 distinct 10 cell ensembles stimulations from the same recording. Trial variability presented as mean  $\pm$  99% c.i.. Significantly modulated conditions (i.e., 99% c.i. excludes 0) are marked in red. **B:** All non-target cells from a given field of view response to a single example hologram. Mean  $\pm$  99% c.i. sorted by mean response. Cells that are significantly modulated (i.e., 99% c.i. excludes 0) marked in red. To this hologram 67 cells were significantly suppressed, while 21 were activated. **C:** For each stimulated ensemble, the fraction of non-target cells significantly activated (blue) or suppressed (orange) (via 99% c.i.) is presented as a histogram. False discovery rate (1%) is noted by the dotted red line. N=160 Ensembles, 18 FOVs, 13 Mice. **D:** An example pair of cells that were close to each other ( $<30\mu\text{m}$ ) but responded differently to different, but similar, ensembles. Cell A (purple) was targeted in both Ensemble 1 (top) and Ensemble 2 (bottom). Cell B (green) was never directly targeted but was silent in ensemble 1 and driven in ensemble 2. Each row shows a schematic of the ensemble (far left), color plot of the fluorescence observed each trial for cell A (left), mean  $\pm$  95% c.i. response for cell A (middle), color plot of the fluorescence observed each trial for cell B (right), and mean  $\pm$  95% c.i. response for cell B (far right).

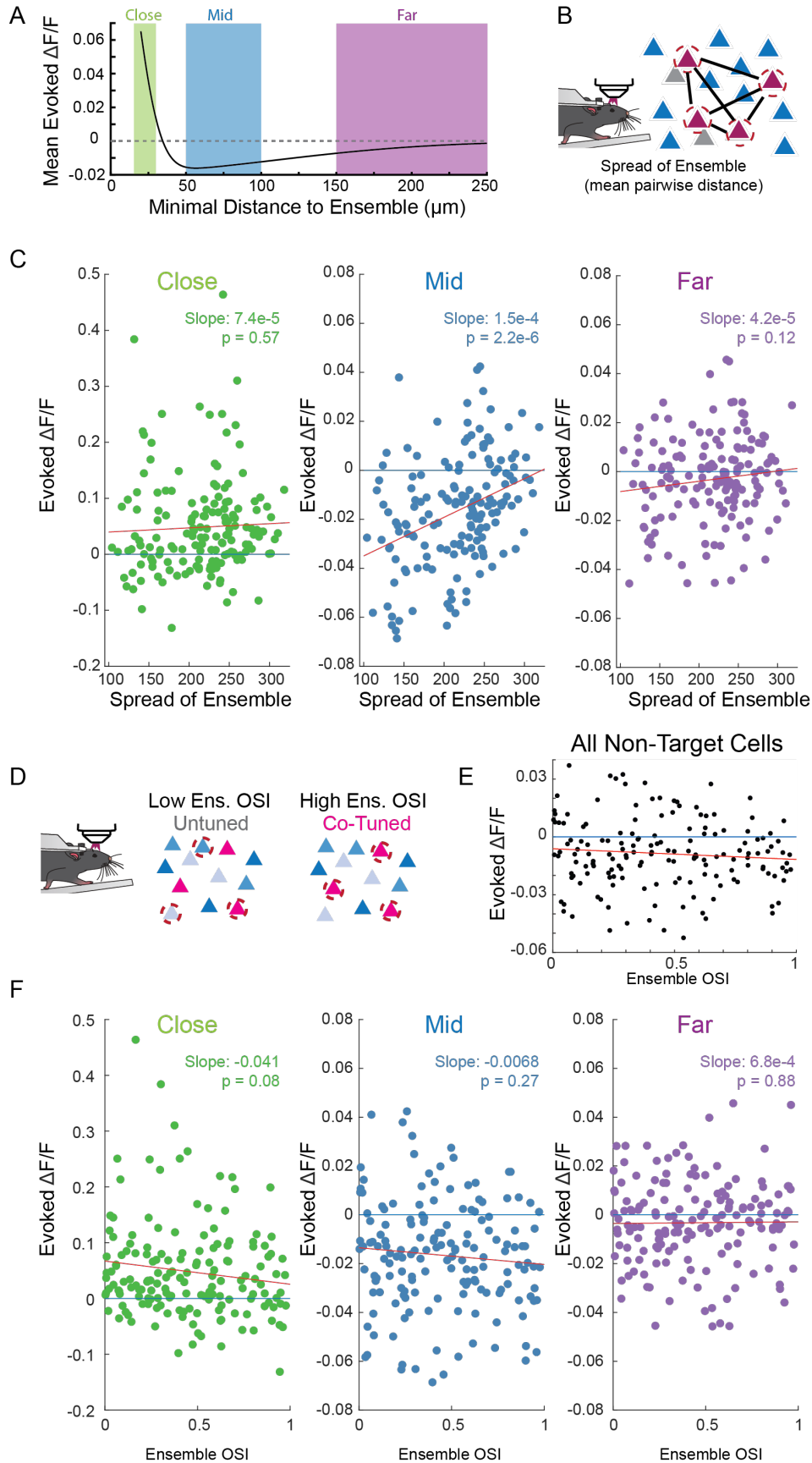


**SFig 4: Observed decrease in fluorescence is dependent on the number of spikes added.** **A:** Number of total pulses added increased overall mean suppression. Mean evoked population response to 10 cell ensemble stimulation, with 1, 5, 10 or 50 pulses per cell.  $P < 1.97E-7$  ANOVA, N=76 Ensembles, 5 FOVs, 2 Mice. **B:** Rate of stimulation did not affect the overall mean suppression. Mean evoked population response to 10 cell ensemble driven with 10 pulses at 3, 10, 30 or 50 Hz.  $P > 0.74$  ANOVA, N=46 Ensembles 2 FOVs, 2 Mice. **C:** Number of cells stimulated, when holding number of spikes constant, did not change overall suppression. Ensembles of 33 cells driven with 3 pulses, vs 10 cells driven with 10 pulses, vs 3 cells driven with 33 pulses did not recruit a differential amount of suppression.  $P > 0.78$  ANOVA, N=99 Ensembles, 11 FOVs, 5 Mice.

897



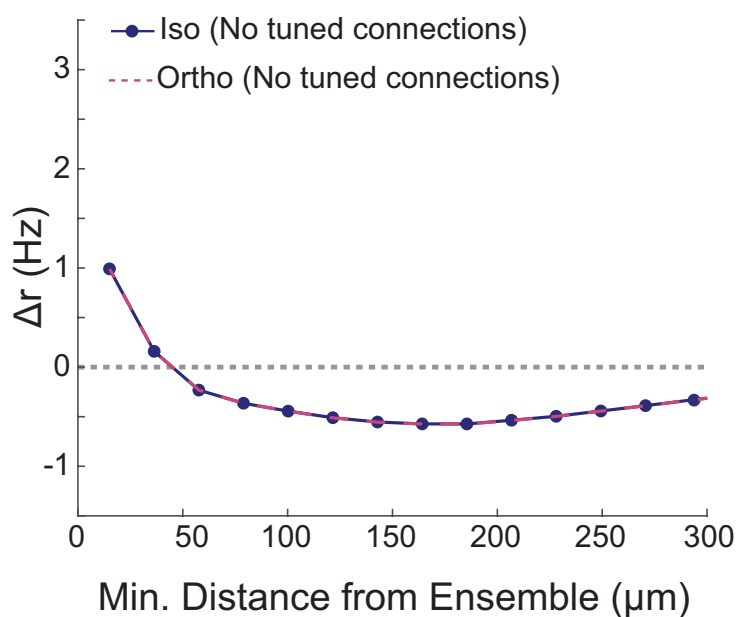
**SFig 5: Using experimental data to fit spatial and feature spread parameters.** **A:** Data from Rossi et al. (2020) used to fit the broad spatial component of  $E \rightarrow \alpha$ , for  $\alpha = E$ ,  $I$  ( $\sigma_{e,b} = 147.31 \mu\text{m}$ ). **B:** Same as A, except for  $I \rightarrow \alpha$  ( $\sigma_{i,b} = 111.27 \mu\text{m}$ ). **C:** Data from Rossi et al. (2020) to fit the feature-based connectivity rule for  $E \rightarrow E$  connections ( $\sigma_{ee} = 21^\circ$ ,  $r_0 = 0.056$ ,  $r_p = 0.084$ ). **D:** Zoomed in portion of panel A from  $0^\circ$  to  $90^\circ$ . **E:** Non-targeted cell responses to optogenetic stimulation as a function of minimal distance to ensemble for different (open circles) fitted to a sum of Gaussian spatial functions for different bin widths. The zero-crossing, maximum, and minimum values were estimated for each fitted function and used to determine the experimentally observed data regime box used in Fig. 2C.



**SFig 6: Correlation of population responses to ensembles statistics. A:** Non-Target cells are categorized based on their proximity to a targeted cell as close ( $< 30 \mu\text{m}$ , green), middle ( $50\text{-}100 \mu\text{m}$ , blue) or far ( $> 150 \mu\text{m}$ , purple) cells. These categories are plotted against the predicted average response from Figure 2A. **B:** Schematic showing the mean pairwise distance of a stimulated ensemble. **C:** Population averages of evoked fluorescence from non-target cells categorized as close (green), middle (blue), or far (purple) from a targeted cell as a function of the ensemble spread. Each dot is a population response to an ensemble,  $N=160$  Ensembles, 18 FOVs, 13 mice. Blue line 0 effect, red line linear regression fit. Slope and linear regression p value written on the plot. **D:** Schematic showing tuned vs untuned ensembles. **E:** The evoked fluorescence from all non-targeted cells regardless of distance to a stimulated cell as a function of ensemble OSI (i.e., tuning). **F:** As in C, but as a function of Ensemble OSI.

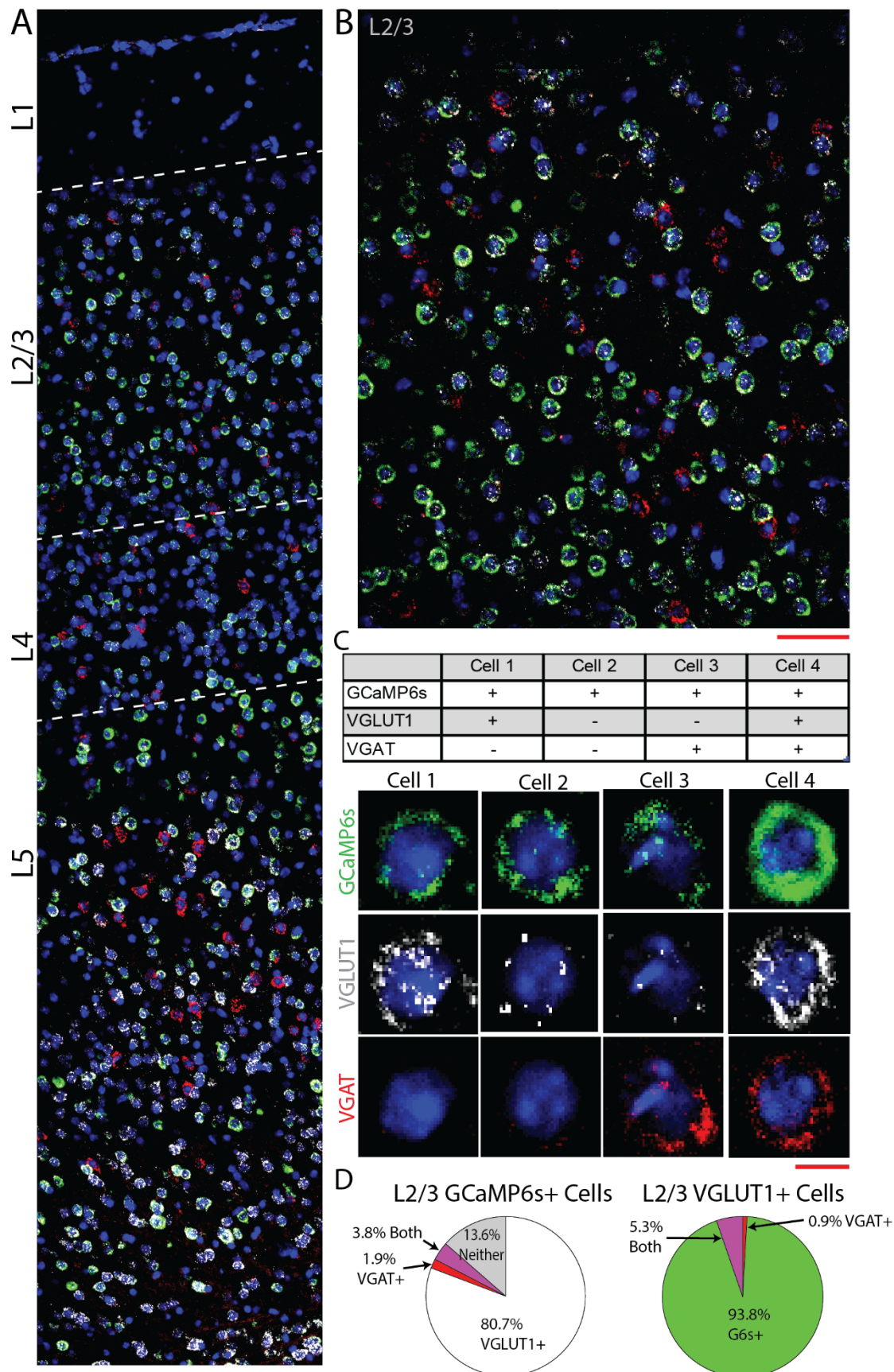
900

901



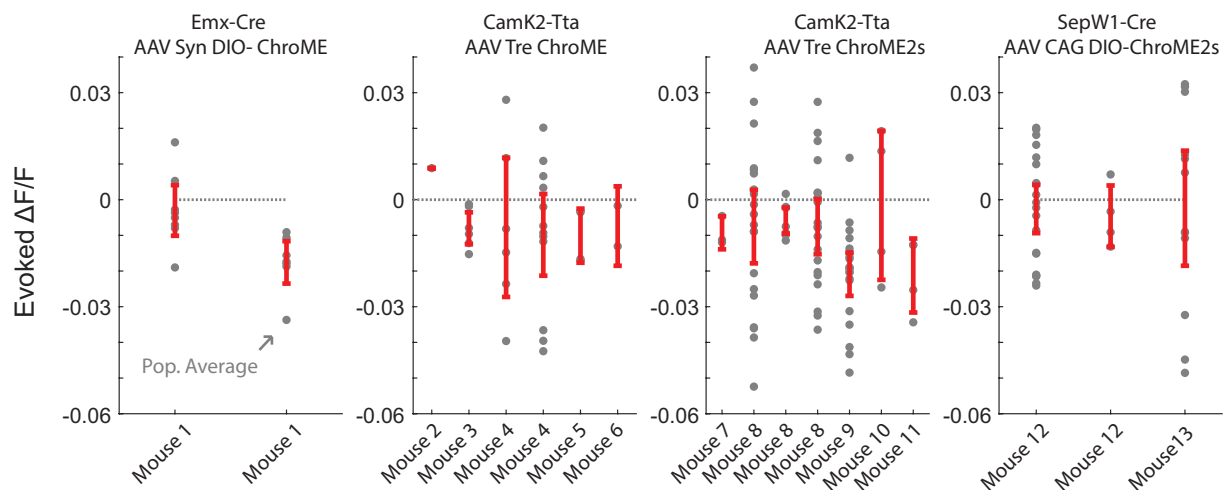
**SFig. 7: Mathematical model with no tuned connections fails to capture experimental observations.** When synaptic connectivity only followed a spatial wiring rule with no specificity in orientation space (i.e.,  $h_{\alpha}(\theta)=1$ ), there is no difference in the recruited recurrent activity of iso-oriented (solid blue) vs. orthogonally oriented (dashed red) neurons.

902



**SFig 8: RNAscope validation of cell type specificity. A:** A cortical section of a tetO-GCaMP6s x Camk2a-tTA mouse using RNAscope. GCaMP6s (green), VGLUT1 (white), VGAT (red), and DAPI (Blue) are labeled. Approximate division of cortical layers noted by dashed lines. Scale bar 100  $\mu\text{m}$ . **B:** Enlarged view of L2/3 cortex. Scale bar 50  $\mu\text{m}$ . **C:** Example L2/3 cells with expression of GCaMP6s, VGLUT1, and/or VGAT noted. Scale Bar 5  $\mu\text{m}$ . **D:** Quantification of 300 DAPI positive cells, presented as either GCaMP6s+ cells that co stained for markers of VGLUT1, VGAT, or both (left) or VGLUT1+ cells that co-stain for GCaMP6s, VGAT, or both (right). 84.5% of GCaMP6s+ cells stain for VGLUT1, 99.1% of VGLUT1+ cells stain for GCaMP6s.

904



**SFig 9: Comparison of effects by mouse and preparation.** Mean population average of all non-targeted cells in response to each 10 cell ensemble stimulation (grey dot). Average  $\pm$  SEM for each recording FOV in red. Divided by expression selectivity driver (Emx-cre, CamK2-tTA, or SepW1-Cre) and viral construct (Syn-DIO-ChroME, Tre-ChroME, Tre-ChroME2s, or CAG DIO-ChroME2s). Note SepW1-Cre ensembles are more likely to be spread out, due to the sparse nature.

905